JCTC Journal of Chemical Theory and Computation

pubs.acs.org/JCTC Article

Probing Molecular Chirality of Ground and Electronically Excited States in the UV−vis and X-ray Regimes: An EOM-CCSD Study

Josefine H. Andersen, Kaushik D. Nanda, Anna I. Krylov, and Sonia Coriani*

Cite This: *J. Chem. Theory Comput.* 2022, 18, 1748−1764 Read Online

ACCESS | Metrics & More | Article Recommendations | Supporting Information

ABSTRACT: We present several strategies for computing electronic circular dichroism (CD) spectra across different frequency ranges at the equation-of-motion coupled-cluster singles and doubles level of theory. CD spectra of both ground and electronically excited states are discussed. For selected cases, the approach is compared with coupled-cluster linear response results as well as time-dependent density functional theory. The extension of the theory to include the effect of spin−orbit coupling is presented and illustrated by calculations of X-ray CD spectra at the *L*-edge.

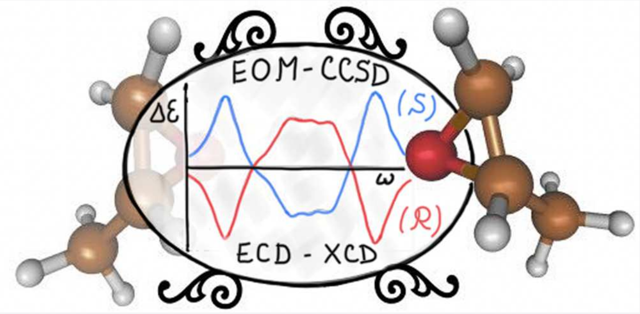

1. INTRODUCTION

An object is chiral if its mirror images cannot be brought into coincidence by rotation. In molecules, chirality typically arises either due to the presence of chiral centers, i.e., asymmetrically substituted tetrahedral centers, or due to the handedness of a helical structure (axial chirality), which makes clockwise and counterclockwise structures nonsuperimposable. The isomers with nonsuperimposable mirror structures are called enantiomers, whereas those that are nonsuperimposable and are not mirror images are named diastereomers.[1]

Chirality is a common and important molecular property with broad consequences. On a molecular level, many biological objects, such as sugars, amino acids, and secondary structures of proteins and nucleic acids, are chiral. Thus, chirality makes living beings enantio-sensitive. This is critically important for the pharmaceutical and food industry because different enantiomers have drastically different biological effects: e.g., left-handed sugars taste bitter; different enantiomers of the same drug may have different pharmacological effects, the thalidomide tragedy[2] being a never-fading reminder. Any prospective new drug based on a chiral structure must have clearly assigned absolute configuration.

Also fascinating, life is homochiral—in living organisms, chiral biological molecules exist almost exclusively as single enantiomers. For example, all naturally occurring chiral amino acids are left-handed and all naturally occurring sugars are right-handed. The origin of the homochirality in life remains an unsolved mystery: when synthesized in the lab, left- and right-handed molecules of a compound most often form a racemic mixture, implying that primordial processes in Nature must have been driven by a directing (chiral) template.[3]

Opposite enantiomers have practically the same energy spectrum; hence, they cannot be distinguished by simple absorption of linearly polarized light. A pseudoscalar effect is needed, such as the differential interaction with the left or right circularly polarized components of linearly polarized light. Differential transmission results in oppositely signed rotation of the plane of polarization, which is exploited in optical rotation (OR) measurements. Even more powerful is the technique of measuring the differential absorption of the two circularly polarized components, which is the basis of circular dichroism spectroscopies.[4] In electronic circular dichroism (ECD),[4,5] the probing light activates electronic transitions in the sample, most typically in the UV−visible frequency region, where valence excitations occur. X-ray radiation can also be used, in principle, to probe chirality via excitations of core electrons. In vibrational circular dichroism (VCD),[1,4,6] infrared light is used to probe dichroism effects in vibrational transitions of the enantiomers in their ground states. An emerging chiral rotational spectroscopy exploits dichroism effects using microwave (MW-CD) radiation.[7−9] Chirality can also be probed by transitions to the continuum, as done in photoelectron circular dichroism.[10,11]

The key step in contemporary use of spectroscopy for chiral discrimination is the simulation of the spectra for an *a priori* chosen absolute configuration of the chiral species.[12,13] Indeed, experimental measurements of optical activity alone are not sufficient to establish the absolute configuration, since there is

Received: September 17, 2021
Published: February 21, 2022

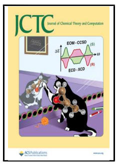

https://doi.org/10.1021/acs.jctc.1c00937

no direct correspondence between the enantiomer's configuration and the measured sign of the chiroptical property. However, if the simulated spectrum of the chosen configuration matches the sign pattern of the measured spectrum, one can conclude that the experimental sample contains the same enantiomer as in the simulation,[5,12−14] provided, of course, that the computational method is reliable.

The appeal of this strategy has stimulated the development of reliable computational methods to simulate ORD, ECD, and VCD spectra. Time-dependent density functional theory approaches (TDDFT) are undoubtedly playing the leading role in this endeavor,[5,12] but the need for alternative, wave function-based methods has been highlighted on many occasions—at the very least, to provide a reliable benchmark against which the validity and accuracy of TDDFT can be checked.[15−19]

Equation-of-motion coupled-cluster theory (EOM-CC)[20−23] and the closely related coupled-cluster response theory (CC-RSP)[18,24,25] are popular and robust theoretical frameworks for simulating spectroscopy. The portfolio of spectroscopies that can be treated using EOM-CC/CC-RSP methods is vast and expanding. Spanning linear and nonlinear regimes, as well as different frequency ranges of probing radiation, it comprises UV−vis one- and two-photon absorption[26−28] and dichroism,[29] magnetic circular dichroism,[30,31] X-ray absorption,[32] dichroism[33] and photoemission,[32,34] resonant inelastic X-ray scattering,[33,35,36] and many more. The non-Hermitian (bivariational) nature of the underlying formalism has initially posed some complications (compared to Hermitian variational methods) for modeling natural optical activity, but solutions have been proposed for dealing with issues such as gauge-invariance and gauge-origin dependency.[37,38]

In this work, we focus on EOM-CC theory, specifically, the EOM-CC model with singles and doubles (EOM-CCSD),[20] as the theoretical framework for computing electronic circular dichroism spectra. We consider the calculation of ECD both in the UV−vis and in the X-ray frequency regimes. The latter requires using specific techniques to treat the core-level transitions—for that purpose, we employ our frozen-core core−valence-separated (fc-CVS) EOM-CC approach.[32] In addition to the ECD of molecules in their ground states, we also simulate excited-state circular dichroism, i.e., the ECD spectra of electronically excited species, needed for the simulation of time-resolved/pump−probe experiments employing circular dichroism as the probe.[39−43] So far, theoretical studies of excited-state ECD have been limited to the TDDFT[43,44] and algebraic diagrammatic construction (ADC) levels of theory.[45]

Although the fundamental equations for simulating ECD using EOM-CCSD have been known for decades, only CC-RSP appears to have been used,[16,17,46−49] maybe because of a fear of the "lack of size-intensivity" of the EOM-CCSD transition moments.[50,51] However, whether this trait of the theory has any serious practical consequences in calculations of ECD spectra has not been explored; we consider this issue here by comparing EOM-CCSD with CC-RSP results. An advantage of EOM-CC over CC-RSP is that EOM-CC does not require solving additional response equations (for the excited-state multipliers) and performing additional matrix transformations, thus resulting in a computationally slightly less expensive approach. As computing the extra response amplitudes in the CC-RSP approach can become tricky, especially in the high-energy regime, the EOM-CC approach is less prone to divergences. Furthermore, the EOM-CC approach avoids the spurious poles originating from the T-amplitude response, which plague the transition and excited-state properties computed with the CC-RSP approach.[52]

The paper is organized as follows. In the theory section, we recapitulate the general definitions of the ECD spectroscopic parameters and observables and then discuss strategies for computing them within EOM-CCSD and CCSD-RSP. This encompasses both the calculation of "stick spectra" (i.e., excitation energies and ECD rotatory strengths) and the direct calculation of the ECD cross sections via damped response theory. We then present illustrative results for ECD of ground and excited states of methyloxirane, norcamphor, and binol. We also discuss the exemplary X-ray CD results for methyloxirane and L-alanine at the K-edge and chloroethanol at the L-edge of chlorine, with and without the inclusion of spin−orbit splitting. Concluding remarks are given at the end.

2. THEORY

2.1. Definitions.

For isotropic samples, CD spectra are typically obtained by calculating the rotatory strengths R_{nf} for the electronic transitions $n \rightarrow f$ ($n = 0$ for the ground state). In the length gauge (labeled lg), these are defined as the scalar products (Rosenfeld equation)

$$R_{nf}^{\mathrm{lg}} = \sum_{\alpha=x,y,z} \mathfrak{I}\langle n|\hat{\mu}_\alpha|f\rangle\langle f|\hat{m}_\alpha|n\rangle = \frac{1}{2}\sum_{\alpha=x,y,z} \mathfrak{I}\langle n|\hat{r}_\alpha|f\rangle\langle f|\hat{L}_\alpha|n\rangle \tag{1}$$

where $\mathfrak{I}$ stands for the imaginary part, and $\hat{\mu}_\alpha$ and $\hat{m}_\alpha$ are the Cartesian components of the electric dipole and magnetic dipole operators, respectively. In atomic units (a.u.), $\hat{\boldsymbol{\mu}} = -\hat{\boldsymbol{r}}$ and $\hat{\boldsymbol{m}} = -\frac{1}{2}\hat{\boldsymbol{L}}$, where $\hat{\boldsymbol{r}}$ is the position operator, $\hat{\boldsymbol{L}} = \hat{\boldsymbol{r}} \times \hat{\boldsymbol{p}} = -i\hat{\boldsymbol{r}} \times \hat{\nabla}$ is the orbital angular momentum, and $\hat{\boldsymbol{p}} = -i\hat{\nabla}$ is the linear momentum. By exploiting Ehrenfest's off-diagonal hypervirial relationship (in a.u.)[15,53,54]

$$i\langle n|\hat{\boldsymbol{p}}|f\rangle = \langle n|[\hat{\boldsymbol{r}}, \hat{H}]|f\rangle = \omega_{fn}\langle n|\hat{\boldsymbol{r}}|f\rangle \tag{2}$$

where $\omega_{fn} = (E_f - E_n)$ is the energy difference between the two states, one obtains the rotatory strength in the velocity gauge (abbreviated vg)

$$R_{nf}^{\mathrm{vg}} = \frac{1}{\omega_{fn}}\sum_{\alpha=x,y,z} \mathfrak{R}\langle n|\hat{p}_\alpha|f\rangle\langle f|\hat{m}_\alpha|n\rangle = -\frac{1}{2\omega_{fn}}\sum_{\alpha=x,y,z} \mathfrak{R}\langle n|\hat{p}_\alpha|f\rangle\langle f|\hat{L}_\alpha|n\rangle \tag{3}$$

where $\mathfrak{R}$ indicates the real part.

The dipole oscillator strength f of one-photon absorption (OPA) can also be expressed in different gauges—length, velocity, and mixed (mx):[55]

$$f^{\mathrm{lg}} = \frac{2\omega_{fn}}{3}\sum_\alpha \langle n|\hat{\mu}_\alpha|f\rangle\langle f|\hat{\mu}_\alpha|n\rangle \tag{4}$$

$$f^{\mathrm{vg}} = \frac{2}{3\omega_{fn}}\sum_\alpha \langle n|\hat{p}_\alpha|f\rangle\langle f|\hat{p}_\alpha|n\rangle \tag{5}$$

$$f^{\mathrm{mx}} = \frac{2i}{3}\sum_\alpha \langle n|\hat{\mu}_\alpha|f\rangle\langle f|\hat{p}_\alpha|n\rangle \tag{6}$$

2.2. EOM-CC Theory for Valence and Core-Level States. The (ground-state) coupled-cluster wave function (Ψ_{CC}) is given in terms of the exponential of the cluster operator $\hat{T}$ acting on the reference (usually, Hartree−Fock) Slater determinant Φ_0:[56]

$$|\Psi_{\text{CC}}\rangle \equiv |\Psi_0\rangle = e^{\hat{T}}|\Phi_0\rangle \tag{7}$$

At the CCSD level, the second-quantization form of $\hat{T}$ reads

$$\hat{T} = \hat{T}_1 + \hat{T}_2; \quad \hat{T}_1 = \sum_{ia} t_i^a \hat{a}_a^\dagger \hat{a}_i; \quad \hat{T}_2 = \frac{1}{4}\sum_{ijab} t_{ij}^{ab} \hat{a}_a^\dagger \hat{a}_b^\dagger \hat{a}_j \hat{a}_i \tag{8}$$

where t_i^a and t_{ij}^{ab} are cluster amplitudes associated with singles and doubles excitations, and $\hat{a}_i$, $\hat{a}_a^\dagger$ are (electron) annihilation and creation operators, respectively. We adopt the standard notation, where indices $i, j, k, \cdots$ refer to occupied, $a, b, c, \cdots$ to virtual, and $p, q, r, \cdots$ to general molecular spin−orbitals; the separation between the occupied and virtual orbital spaces is determined by the choice of the reference determinant Φ_0. The cluster amplitudes satisfy the CC equations

$$\langle \Phi_\nu | \bar{H} | \Phi_0 \rangle = 0 \tag{9}$$

where, for CCSD, Φ_ν spans the singles and doubles excitation manifold. $\bar{H} = e^{-\hat{T}}\hat{H}e^{\hat{T}}$ is the similarity-transformed Hamiltonian.

The EOM-CCSD target state n is expressed using the (right) EOM operator $\hat{\mathcal{R}}^n$ acting on the CCSD wave function as follows:

$$|\Psi_n\rangle = \hat{\mathcal{R}}^n \Psi_{\text{CC}} = \hat{\mathcal{R}}^n e^{\hat{T}} |\Phi_0\rangle \tag{10}$$

The type of target states determines the choice of $\hat{\mathcal{R}}$. $\hat{\mathcal{R}}$ accesses a specific sector of the Fock space defined by the set of target determinants, relative to the reference determinant. Within EOM-CCSD for excitation energies (EOM-EE-CCSD), $\hat{\mathcal{R}}^n$ accesses the reference and valence singly and doubly excited configurations:

$$\hat{\mathcal{R}} = r_0 + \sum_{ia} r_i^a \hat{a}_a^\dagger \hat{a}_i + \frac{1}{4}\sum_{ijab} r_{ij}^{ab} \hat{a}_a^\dagger \hat{a}_b^\dagger \hat{a}_j \hat{a}_i \tag{11}$$

where r_0, r_i^a, and r_{ij}^{ab} are the EOM-EE-CCSD amplitudes satisfying the following eigenvalue equation:

$$\bar{H}\hat{\mathcal{R}}^n|\Phi_0\rangle = E_n \hat{\mathcal{R}}^n |\Phi_0\rangle \tag{12}$$

The state with $r_0 = 1$ and $r_i^a = r_{ij}^{ab} = 0$ $\forall\{i,j,a,b\}$ is the reference CCSD state ($n = 0$, usually, but not always, the ground state), and the rest ($n > 0$) are EOM-CC target states (e.g., valence excited states). In a similar fashion, target core-excited states can be computed from the EOM-CCSD eigenvalue equation by restricting the EOM-CCSD operator to only access the core-excited configurations.[32,57] In the here-adopted core−valence-separated EOM-EE-CCSD approach with frozen−core approximation (fc-CVS-EOM-EE-CCSD),[32] this corresponds to

$$\hat{\mathcal{R}} = \sum_{Ia} r_I^a \hat{a}_a^\dagger \hat{a}_I + \frac{1}{2}\sum_{Ijab} r_{Ij}^{ab} \hat{a}_a^\dagger \hat{a}_b^\dagger \hat{a}_j \hat{a}_I + \frac{1}{4}\sum_{IJab} r_{IJ}^{ab} \hat{a}_a^\dagger \hat{a}_b^\dagger \hat{a}_J \hat{a}_I \tag{13}$$

where capital labels I and J denote core orbitals. In contrast to the CVS scheme employed by Coriani and Koch,[57] in the fc-CVS-EOM-EE-CCSD approach of Vidal et al.,[32] the core orbitals are frozen (uncorrelated) in the ground-state calculation.

Within the non-Hermitian EOM-CC theory, the left and right eigenfunctions of $\bar{H}$ are not complex conjugates of each other. The left eigenfunctions are obtained from the left EOM-CC eigenvalue equation

$$\langle \Phi_0 | \hat{\mathcal{L}}^n \bar{H} = \langle \Phi_0 | \hat{\mathcal{L}}^n E_n \tag{14}$$

where $\hat{\mathcal{L}}^n$ is the left EOM-CC operator. The left EOM-EE-CCSD and fc-CVS-EOM-EE-CCSD (de-excitation) operators are defined according to

$$\hat{\mathcal{L}} = l_0 + \sum_{ia} l_i^a \hat{a}_i^\dagger \hat{a}_a + \frac{1}{4}\sum_{ijab} l_{ij}^{ab} \hat{a}_i^\dagger \hat{a}_j^\dagger \hat{a}_b \hat{a}_a \tag{15}$$

and

$$\hat{\mathcal{L}} = \sum_{Ia} l_I^a \hat{a}_I^\dagger \hat{a}_a + \frac{1}{2}\sum_{Ijab} l_{Ij}^{ab} \hat{a}_I^\dagger \hat{a}_j^\dagger \hat{a}_b \hat{a}_a + \frac{1}{4}\sum_{IJab} l_{IJ}^{ab} \hat{a}_I^\dagger \hat{a}_J^\dagger \hat{a}_b \hat{a}_a \tag{16}$$

respectively. In the context of the left ground-state reference, $\hat{\mathcal{L}}$ is historically referred to as $1 + \hat{\Lambda}$ according to

$$\langle \tilde{\Psi}_n | = \langle \Phi_0 | (1 + \hat{\Lambda}) e^{-\hat{T}}; \qquad \hat{\Lambda} = \sum_{\mu \neq \Phi_0} \lambda_\mu \hat{\tau}_\mu^\dagger \tag{17}$$

Note that $l_0 = 1$ for the reference ($n = 0$) CCSD state and $l_0 = 0$ for the EOM-CC states. In the literature, the ground-state left amplitudes are also often denoted as $\bar{t}_\mu$ to highlight that they are Lagrangian multipliers of the right amplitudes t_μ.[25]

The EOM-CC left and right eigenvectors can be normalized to form a biorthonormal set, such that $\langle \hat{\mathcal{L}}^n | \hat{\mathcal{R}}^m \rangle = \delta_{nm}$, where δ_{nm} is the Kronecker delta.

2.3. EOM-CCSD Rotatory Strengths: Density-Based Implementation. Within the non-Hermitian CC theory, the right ($\langle \hat{O}^{fn} \rangle$) and left ($\langle \hat{O}^{nf} \rangle$) transition moments between different states are not equal; here, $\hat{O}$ is a general operator. As a result, the expressions for the rotatory strengths (as those for the oscillator strengths) are explicitly symmetrized with respect to complex conjugation (denoted by *)

$$\begin{aligned} R_{nf}^{\text{lg}} &= \frac{1}{2}\sum_\alpha \left\{ \frac{1}{2}(\langle \hat{r}_\alpha^{nf} \rangle \langle \hat{L}_\alpha^{fn} \rangle + \langle \hat{L}_x^{nf} \rangle^* \langle \hat{r}_\alpha^{fn} \rangle^*) \right\} \\ &= \frac{1}{4}\sum_\alpha \{ \langle \hat{r}_\alpha^{nf} \rangle \langle \hat{L}_\alpha^{fn} \rangle - \langle \hat{L}_\alpha^{nf} \rangle \langle \hat{r}_\alpha^{fn} \rangle \} \end{aligned} \tag{18}$$

$$R_{nf}^{\text{vg}} = -\frac{1}{4\omega_{nf}}\sum_\alpha \{ \langle \hat{p}_\alpha^{nf} \rangle \langle \hat{L}_\alpha^{fn} \rangle + \langle \hat{L}_\alpha^{nf} \rangle \langle \hat{p}_\alpha^{fn} \rangle \} \tag{19}$$

The right and left transition moments can be computed as

$$\langle \hat{O}^{fn} \rangle = \langle \Phi_0 \hat{\mathcal{L}}^f e^{-\hat{T}} | \hat{O} | e^{\hat{T}} \hat{\mathcal{R}}^n \Phi_0 \rangle = \sum_{pq} \gamma_{pq}^{f \leftarrow n} O_{pq} \tag{20}$$

$$\langle \hat{O}^{nf} \rangle = \langle \Phi_0 \hat{\mathcal{L}}^n e^{-\hat{T}} | \hat{O} | e^{\hat{T}} \hat{\mathcal{R}}^f \Phi_0 \rangle = \sum_{pq} \gamma_{pq}^{n \leftarrow f} O_{pq} \tag{21}$$

where $\gamma^{f \leftarrow n}$ and $\gamma^{n \leftarrow f}$ are the right and left reduced transition one-particle density matrices (1PDMs), respectively; O_{pq} is the matrix representation of the operator in the MO basis (i.e., property integrals). The programmable expressions for the transition 1PDMs between different EOM-CCSD target states used in this study are presented in the Appendix and also reported elsewhere.[20,32]

2.4. EOM-CCSD Rotatory Strengths: Alternative Implementation. Within CC-RSP theory, the transition moments are often expressed as contractions of fundamental CC building blocks[24,25]

$$\langle \hat{O}^{f0} \rangle_{\mathrm{rsp}} = \sum_{\mu} l_{\mu}^{f} \xi_{\mu}^{O} \tag{22}$$

$$\langle \hat{O}^{0f} \rangle_{\mathrm{rsp}} = \sum_{\mu} \eta_{\mu}^{O,\mathrm{rsp}} r_{\mu}^{f} + \sum_{\mu} \bar{M}_{\mu}^{f}(\omega_f) \xi_{\mu}^{O} \tag{23}$$

$$\langle \hat{O}^{kj} \rangle_{\mathrm{rsp}} = \sum_{\mu\nu} l_{\mu}^{k} A_{\mu\nu}^{O,\mathrm{rsp}} r_{\nu}^{j} + \sum_{\mu} \bar{N}_{\mu}^{kj}(\omega_k, \omega_j) \xi_{\mu}^{O} \tag{24}$$

where

$$\xi_{\mu}^{O} = \langle \Phi_{\mu} | e^{-\hat{T}} \hat{O} e^{\hat{T}} | \Phi_0 \rangle \tag{25}$$

$$A_{\mu\nu}^{O,\mathrm{rsp}} = \langle \Phi_{\mu} | [e^{-\hat{T}} \hat{O} e^{\hat{T}}, \hat{\tau}_{\nu}] | \Phi_0 \rangle \tag{26}$$

$$\eta_{\mu}^{O,\mathrm{rsp}} = \langle \Phi_0 | [e^{-\hat{T}} O e^{\hat{T}}, \hat{\tau}_{\mu}] | \Phi_0 \rangle + \sum_{\lambda} \bar{t}_{\lambda} A_{\lambda\mu}^{O,\mathrm{rsp}} \tag{27}$$

Above, $\bar{M}_{\mu}^{f}(\omega_f)$ and $\bar{N}_{\mu}^{kj}(\omega_k,\omega_j)$ are excited-state Lagrangian multipliers.[25] Greek indices refer to the excitation levels (here either singles or doubles) and $\hat{\tau}_{\mu}$ is the corresponding excitation operator. Note the superscripts f and k to distinguish between the excited state amplitudes r_{μ} and l_{μ}.

Analogous expressions can be written for the EOM-CCSD transition moments[35,50,58]

$$\langle \hat{O}^{f0} \rangle = \sum_{\mu} l_{\mu}^{f} \xi_{\mu}^{O} \tag{28}$$

$$\langle \hat{O}^{0f} \rangle = \sum_{\mu} \eta_{\mu}^{O} r_{\mu}^{f} \tag{29}$$

$$\langle \hat{O}^{kj} \rangle = \sum_{\mu\nu} l_{\mu}^{k} A_{\mu\nu}^{O} r_{\nu}^{j} - \left(\sum_{\rho} \bar{t}_{\rho} \xi_{\rho}^{O}\right) \delta_{kj} - \left(\sum_{\rho} l_{\rho}^{k} \xi_{\rho}^{O}\right)\left(\sum_{\rho} \bar{t}_{\rho} r_{\rho}^{j}\right) \tag{30}$$

where the EOM-CCSD building blocks are[35]

$$\eta_{\mu}^{O} = \langle \Phi_0 | e^{-\hat{T}} \hat{O} e^{\hat{T}} | \Phi_{\mu} \rangle + \sum_{\lambda} \bar{t}_{\lambda} \langle \Phi_{\lambda} | e^{-\hat{T}} \hat{O} e^{\hat{T}} | \Phi_{\mu} \rangle - \langle \hat{O} \rangle_{\mathrm{CC}} \bar{t}_{\mu} \tag{31}$$

$$= \langle \Phi_0 | e^{-\hat{T}} \hat{O} e^{\hat{T}} | \Phi_{\mu} \rangle + \sum_{\lambda} \bar{t}_{\lambda} A_{\lambda\mu}^{O} \tag{32}$$

$$A_{\lambda\mu}^{O} = \langle \Phi_{\lambda} | e^{-\hat{T}} \hat{O} e^{\hat{T}} | \Phi_{\mu} \rangle - \delta_{\lambda\mu} \langle \Phi_0 | e^{-\hat{T}} \hat{O} e^{\hat{T}} | \Phi_0 \rangle \tag{33}$$

and $(\sum_{\rho} \bar{t}_{\rho} r_{\rho}^{j}) = -r_0^{j}$.

Simple manipulations connect the CC response and the EOM building blocks[35]

$$\eta_{\mu}^{O} = \eta_{\mu}^{O,\mathrm{rsp}} + \sum_{\mu>\nu} \bar{t}_{\mu} \langle \Phi_{\mu} | \hat{\tau}_{\nu} e^{-\hat{T}} \hat{O} e^{\hat{T}} | \Phi_0 \rangle - \left(\sum_{\rho} \bar{t}_{\rho} \xi_{\rho}^{O}\right) \bar{t}_{\mu} \tag{34}$$

$$A_{\lambda\mu}^{O} = A_{\lambda\mu}^{O,\mathrm{rsp}} + \langle \Phi_{\mu} | \hat{\tau}_{\nu} e^{-\hat{T}} \hat{O} e^{\hat{T}} | \Phi_0 \rangle (1 - \delta_{\mu\nu}) \tag{35}$$

2.5. EOM-CCSD ECD Spectra from the Damped Optical Rotation Tensor. CD spectra can also be obtained directly from the absorbing component of the electric dipole–magnetic dipole optical rotation tensor, $G'_{\alpha\beta}(g)$,[1]

$$\Delta\epsilon \propto -\frac{1}{3} \omega \mu_0 l N G'_{\alpha\alpha}(g) \tag{36}$$

Within damped linear response theory,[33,35,49,59−63] the latter corresponds, in the length gauge, to

$$G_{\alpha\beta}^{\prime,\mathrm{lg}}(-\omega, \omega) \propto \Re \langle\langle \hat{m}_{\alpha}; \hat{\mu}_{\alpha} \rangle\rangle_{\omega+i\gamma} \tag{37}$$

and to

$$G_{\alpha\beta}^{\prime,\mathrm{vg}}(g) \propto \omega^{-1} \Im \langle\langle \hat{m}_{\alpha}; \hat{p}_{\alpha} \rangle\rangle_{\omega+i\gamma} \tag{38}$$

in the velocity gauge; γ is the damping term, which can be regarded as a common inverse lifetime of all excited states. Note that the computation of the ECD spectrum from the absorptive component of the complex optical rotation tensor does not require the use of the modified velocity gauge,[37] since the imaginary part of the static correction term is trivially zero.[49]

The general sum-over-states expression of a complex linear response function (in a.u.) is[61]

$$\langle\langle \hat{O}_1; \hat{O}_2 \rangle\rangle_{\omega+i\gamma} = -\sum_{k>0} \left\{ \frac{\langle \hat{O}_1^{0k} \rangle \langle \hat{O}_2^{k0} \rangle}{E_k - E_0 - \omega - i\gamma} + \frac{\langle \hat{O}_2^{0k} \rangle \langle \hat{O}_1^{k0} \rangle}{E_k - E_0 + \omega + i\gamma} \right\} \tag{39}$$

In our present implementation, we adopted an asymmetric form for the CC damped rotation tensor.[25,49,64] In the vector–matrix notation of Section 2.4, this reads

$$\langle\langle \hat{X}; \hat{x} \rangle\rangle_{\omega+i\gamma} = \frac{1}{2} \hat{C}^{\pm\omega} \{ \bar{t}^{x}(\omega + i\gamma) \xi^{X} + \eta^{X} t^{x}(\omega + i\gamma) \} \tag{40}$$

where the permutator $\hat{C}^{\pm\omega}$ only acts on the real frequency ω.

Note that, in Q-Chem's notation from refs 65 and 66, $t^{x}(\omega + i\gamma)$ and $\bar{t}^{x}(\omega + i\gamma)$ correspond to the response vectors $X^{x}(\omega + i\gamma)$ and $\tilde{X}^{x}(\omega + i\gamma)$ with the response intermediates η^{x} and ξ^{x} given by

$$\langle \eta^{x} | \Phi_{\rho} \rangle = \langle \tilde{D}^{x} | \Phi_{\rho} \rangle - \langle \tilde{D}^{x} | \Phi_0 \rangle \langle \hat{\Lambda} | \Phi_{\rho} \rangle \tag{41}$$

and

$$\langle \Phi_{\rho} | \xi^{x} \rangle = \langle \Phi_{\rho} | D^{x} \rangle \tag{42}$$

Here, $\langle \tilde{D}^{x} | \Phi_{\rho} \rangle = \langle \Phi_0 (1 + \hat{\Lambda}) | e^{-\hat{T}} \hat{x} e^{\hat{T}} | \Phi_{\rho} \rangle$ and $\langle \Phi_{\rho} | D^{x} \rangle = \langle \Phi_{\rho} | e^{-\hat{T}} \hat{x} e^{\hat{T}} | \Phi_0 \rangle$ (see eqs 31 and 25).

Equation 40 requires the solution of the damped linear equations for the right response amplitudes, $t^{x}(\omega + i\gamma)$, and the left response multipliers $\bar{t}^{x}(\omega + i\gamma)$ of the same operator x

$$[\mathbf{A} - (\omega + i\gamma)1] t^{x}(\omega + i\gamma) = -\xi^{x} \tag{43}$$

$$\bar{t}^{x}(\omega + i\gamma)[\mathbf{A} + (\omega + i\gamma)1] = -\eta^{x} \tag{44}$$

where **A** is a sub-block of the similarity-transformed Hamiltonian matrix, often referred to as the CC Jacobian

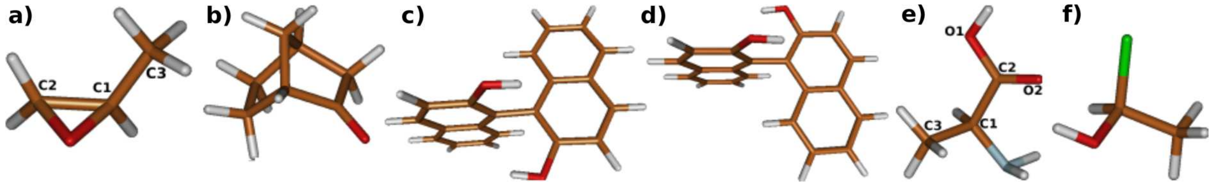

Figure 1. Structures of molecules considered in this work: (a) *R*-methyloxirane, (b) 1*R*-norcamphor, (c) S_a-binol, (d) R_a-binol, (e) L-alanine, and (f) L-chloroethanol. Atom labeling is given when relevant for the discussion of the results.

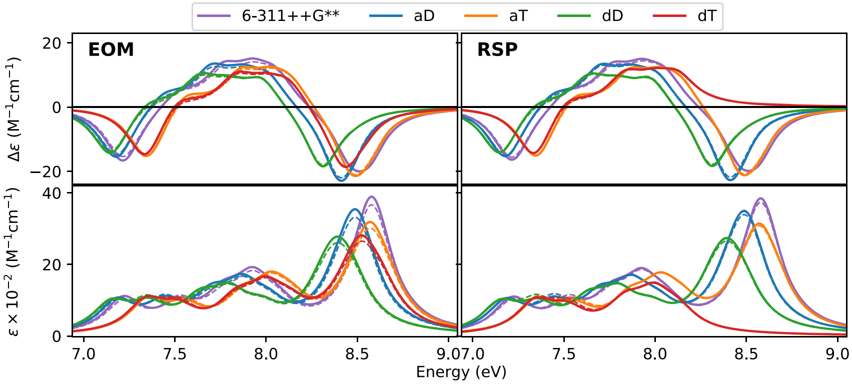

Figure 2. (*R*)-Methyloxirane. EOM-CCSD (left) and CCSD-RSP (right) basis-set study of ground-state transition properties. ECD (top) and OPA (bottom) spectra in length (solid line) and velocity (dashed line) gauges. Lorentzian broadening with HWHM = 0.124 eV. Note that all spectra are based on 8 transitions except the RSP/dT one, which only includes 5 states.

$$\bar{H}_{\mu\nu} = \begin{pmatrix} E_{\mathrm{CC}} & \eta_{\nu} \\ \Omega_{\mu} & A_{\mu\nu} \end{pmatrix} \tag{45}$$

Note that, in contrast to the case of CC linear response, the EOM equations for the response multipliers are decoupled from those for the response amplitudes.[35] The damped response equations (eqs 43−44) can be solved iteratively using damped variants of standard procedures[35,49,63] such as the Direct Inversion in the Iterative Subspace (DIIS) or generalized Davidson.

3. COMPUTATIONAL DETAILS

We implemented the above expressions for the calculation of the electronic circular dichroism within the EOM-CCSD approach in Q-Chem.[67,68] The theory is applicable for valence excitations (EOM-EE-CCSD) as well as core excitations (fc-CVS-EOM-EE-CCSD[32,69]) of both ground and excited states. py-CCRSP[70] was used for code profiling and testing as well as for the damped-response calculations. To illustrate the methodology, we computed various CD spectra for the following systems (shown in Figure 1): (*R*)-methyloxirane, (1*R*)-norcamphor, S_a- and R_a-binol, L-alanine, and L-chloroethanol.

(*R*)-Methyloxirane has previously been used as a model system to computationally investigate excited-state CD (ES-ECD) at the TDDFT level of theory by Rizzo and Vahtras.[44] We use the same geometry as in ref 44. We investigated basis-set effects by employing various correlation-consistent basis sets[71−73] with different augmentation and polarization levels, as well as Pople's 6-311++G** set. The EOM-CCSD results were compared to LR-CCSD results obtained with Dalton.[74] ES-ECD spectra were computed with the d-aug-cc-pVDZ and d-aug-cc-pVTZ basis sets.

For consistency, we used the ground-state geometry of (1*R*)-norcamphor optimized at the DFT/CAM-B3LYP/aug-cc-pVTZ level from ref 45. Ground-state and S_1 excited-state absorption and CD spectra were simulated using the d-aug-cc-pVDZ basis set.

For binol, we considered two structures, namely the S_0 structure of the S_a-isomer from ref 43 and the S_0 structure of the R_a-isomer of ref 45 (including a symmetrized variant). Calculations with the former structure were carried out using the 6-31G* basis set, as was done in ref 43 at the TDDFT level. The 20 lowest excitations in each irrep (*A* and *B* irreps of C_s point group) were computed. The ES-ECD was calculated for the L_a, L_b, and B_b states in each irrep. In the case of the (symmetrized) R_a-isomer, we used the cc-pVDZ basis set, as was done in ref 45 at the ADC(2) and TDDFT levels, and computed the GS-ECD arising from the 20 lowest excitations in each irrep, as well as the ES-ECD of the L_a, L_b, and B_b states. For calculations in the C_1 group, we used a single-precision implementation of CCSD and EOM-CCSD equations.[75]

In the X-ray regime (XCD), we considered, once again, methyloxirane, employing the same geometry for the *R*-isomer as above, as well as a MP2/cc-pVTZ geometry from ref 76. We considered different basis sets, namely, augmented Dunning basis sets as well as standard and uncontracted variants of Pople's 6-311++G** set, which are well-suited for calculations of XAS spectra.[77] The core-excited states of the carbon *K*-edge were computed using the fc-CVS-EOMEE-CCSD scheme in Q-Chem. The linear response results were obtained with the CVS-CCSD scheme in Dalton.[57,74,78]

The XCD of L-alanine was investigated with the d-aug-cc-pVDZ basis set. We computed the *K*-edges of carbon, nitrogen, and oxygen for the neutral and zwitterionic forms of the amino acid. Coordinates for the neutral form were taken from ref 76; the zwitterion structure was obtained from neutron diffraction experiment in ref 79.

Finally, inspired by ref 80, we considered the chlorine *L*-edge of chloroethanol. XAS and XCD spectra with and without

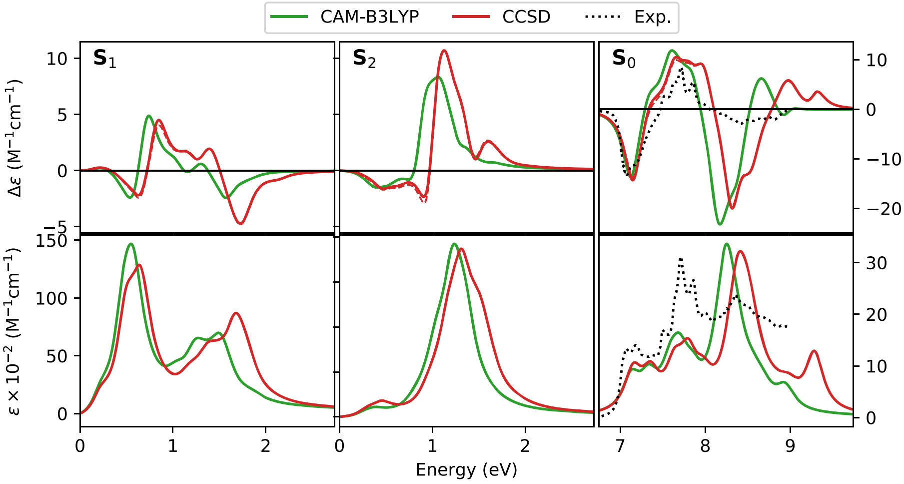

Figure 3. (*R*)-Methyloxirane. Absorption (bottom panel) and CD (upper panel) spectra for S_0, S_1, and S_2. EOM-CCSD and TDDFT/CAM-B3LYP (20 states in both cases) with the d-aug-cc-pVDZ basis set. Dashed line is velocity gauge. Experimental spectra (dotted line) were digitized from ref 82. Lorentzian broadening with HWHM = 0.124 eV.

spin−orbit coupling (SOC) were computed with the 6-311(2+,+)G** basis, specifically uncontracted to describe the 2*p* orbitals of the Cl atom.[69]

Unless otherwise specified, the gauge origin was located at the center of charge, which is the default setup in Q-Chem. RSP-CCSD and TDDFT/CAM-B3LYP results used for comparison were obtained using Dalton.[74,78] Most spectra discussed in the following section were obtained by Lorentzian broadening of the computed stick spectra (excitation energies, oscillator and rotatory strengths), and are reported as decadic molar extinction coefficient for OPA and as extinction coefficient anisotropy for the CD.

4. RESULTS AND DISCUSSION

4.1. UV−vis ECD Spectra. *4.1.1. Methyloxirane.* Methyloxirane (also known as propylene oxide or 1, 2-epoxypropane) is a popular test case for calculations of optical activity in both the UV−vis and X-ray regimes. This chiral organic molecule is small enough for high-level *ab initio* calculations and is also manageable for experimental absorption and circular dichroism studies available in the gas phase.[81,82]

We investigated the basis-set dependence of the ground-state OPA and ECD obtained from the EOM-CCSD and CCSD-RSP calculations. The resulting spectra are shown in Figure 2. See Table S1 for the underlying raw data.

We observe good agreement between the EOM-CCSD rotatory and oscillator strengths obtained from the length and the velocity formulations for all basis sets considered here. The maximum absolute difference between the EOM rotatory strength in the two gauges is 0.004 au for the Pople basis set, 0.003 au for aug-cc-pVDZ and d-aug-cc-pVDZ, and 0.002 au for aug-cc-pVTZ and d-aug-cc-pVTZ. Increasing the basis-set size does not seem to affect this difference, at least not within the sequence of the bases investigated here. However, the quality of the basis moderately affects the peak positions and intensities, although the overall sign pattern is the same for all basis sets. The EOM-CCSD and RSP-CCSD results are nearly identical; the only noticeable difference seen for the d-aug-cc-pVTZ case is due to the smaller number of roots computed in the case of RSP-CCSD.

Next, we examined the performance of EOM-CCSD for calculation of ES-ECD, using the d-aug-cc-pVDZ and d-aug-cc-pVTZ sets, see Tables S2 and S3 in the SI, where transitions from the ground state and from the first 8 excited states up to the twentieth excited state were considered. We immediately note larger differences between the two gauges, now up to 0.09 au in absolute values of the rotatory strength for d-aug-cc-pVDZ and 0.04 au for d-aug-cc-pVTZ. In a few instances, a negative value of the velocity-gauge oscillator strength is obtained. The 6 → 7 transition is also accompanied by a change in sign and magnitude of the rotatory strengths (see Tables S2 and S3). It is important to note, however, that these transitions fall significantly below 0.2 eV (IR-NIR region), which means that numerical instability, resulting from the corresponding small denominators of the order of 0.009 hartree in the vg expressions for oscillator and rotatory strengths, cannot be discounted.

The simulated absorption and CD spectra of the ground state (S_0) and the first two excited states (S_1 and S_2) obtained using the d-aug-cc-pVDZ set are shown in Figure 3, along with the results of TDDFT/CAM-B3LYP/d-aug-cc-pVDZ calculations (the d-aug-cc-pVTZ results are reported in SI, see Figure S2). The experimental spectra for the ground state taken from ref 82 are also shown. The CAM-B3LYP excitation energies are slightly lower than the CCSD ones for all three cases; otherwise, the spectra are qualitatively rather similar. No energy shift was applied. We refer to Tables S4 and S5 for the CAM-B3LYP excitation energies and strengths the corresponding spectra were obtained from. The S_0 spectra agree reasonably well with the available experimental results for *R*-methyloxirane, at least up to 8 eV. Above 8 eV, both computational methods yield a much more intense negative peak than in the experiment, in line with previous findings.[19] Adding Rydberg-type functions to the basis set partly redistributes the intensity over several electronic transitions, yet the third band remains more intense than observed experimentally (see Figure S1 in the SI). Note that the first ionization energy is 10.13 eV (EOM-IP-CCSD/d-aug-cc-pVDZ).

Concluding this section, Figure 4 shows proof-of-principle illustration of our damped-response implementation of the ECD cross section. The trace of the real component of the

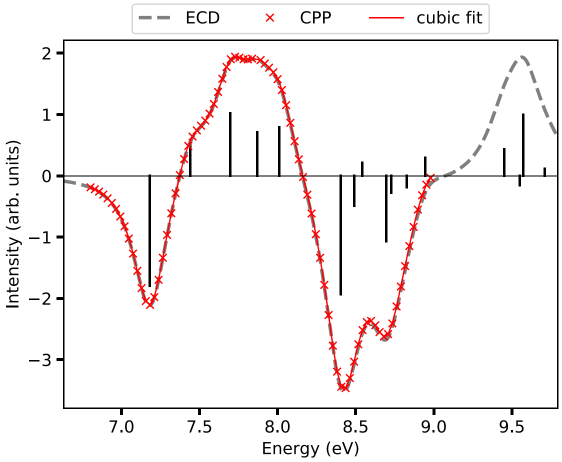

Figure 4. (*R*)-Methyloxirane. EOM-CCSD/aug-cc-pVDZ ground-state ECD spectra obtained from a Lorentzian broadening (HWHM = 0.005 a.u.) of the rotatory strengths (dashed gray line, labelled ECD) and from the damped response function (red grid points and red cubic fit line, labelled CPP) in length gauge.

optical rotation tensor in the length gauge was computed at the frequency grid points indicated by the red X marks and then splined to yield the cross section. The spectrum is practically identical to the one obtained from a Lorentzian broadening of individual rotatory strengths from standard EOM-CCSD theory.

4.1.2. Norcamphor. Moving on to a larger organic molecule, we considered the bicyclic ketone (1*R*)-norcamphor (a.k.a., 2-norbornanone), which has also been investigated in previous theoretical[19,45,83] and experimental[83] gas-phase studies. The ground-state ECD spectra (see right panel of Figure 5) from EOM-CCSD and TDDFT/CAM-B3LYP are rather similar in peak positions, intensities, and sign patterns up to 7.7 eV. Above 7.7 eV, CAM-B3LYP yields a strong negative band, whereas CCSD has a weaker positive peak, followed by a more intense negative one at around 8 eV. The corresponding ADC(3) spectrum of ref 45, also shown in Figure 5, is blue-shifted and has a negative peak centered at around 7.8 eV. Most electronic transitions have been previously assigned *n*s and *n*p characters.[83] When Rydberg-type functions are included, the intensities are redistributed but the overall spectrum remains the same, see Figure S3 and Table S8. The experimental absorption spectrum of the ground state[83] also presents a very weak band centered just above 4 eV, previously assigned to an nπ^* excitation, with a very small positive rotatory strength. We obtain this band at 4.32 eV, with a tiny positive rotatory strength in length gauge and negative strength in velocity gauge. The same behavior was observed at the ADC(3) level. The CAM-B3LYP rotatory strength of the weak nπ^* is positive in both gauges.

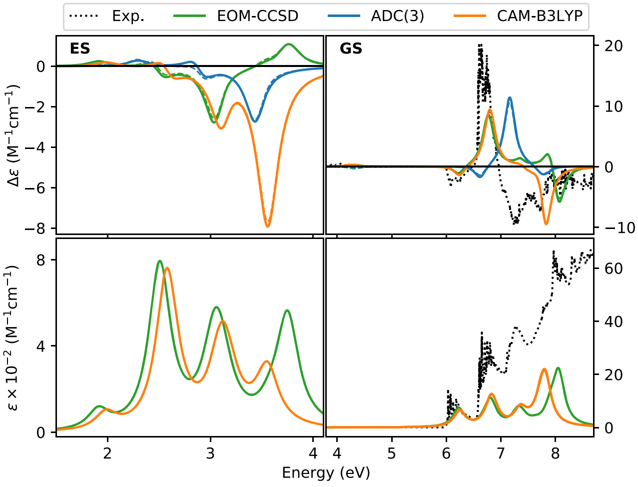

Figure 5. (1*R*)-Norcamphor. S_1 excited-state (ES) and ground-state (GS) ECD (upper panels) and absorption (bottom panels) spectra from EOM-CCSD (this work, 20 states), TDDFT/CAM-B3LYP (this work, 15 states), and ADC(3) (ref 45, 10 states) using the d-aug-cc-pVDZ basis. Dashed lines correspond to velocity gauge. The corresponding EOM-CCSD and TDDFT/CAM-B3LYP OPA and ESA spectra are shown in the two bottom panels. Experimental spectra (dotted line) from ref 83. Lorentzian broadening, HWHM = 0.124 eV.

The shapes of the ECD spectra of the lowest electronic excited state are again similar for all three methods up to 3.5 eV, with an overall blue shift of the ADC(3) spectrum. We note here that we recomputed the CAM-B3LYP ES-ECD spectrum and obtained intensity twice as large as the one reported by Scott et al.[45] Above 3.5 eV, the three methods clearly differ, also because a different number of final states were computed with the three methods (i.e., only 10 states were reported in the ADC(3) study). CAM-B3LYP yields an additional strong negative band and CCSD yields a weaker positive one, reflecting the differences observed in the ground-state spectrum. The raw data of Figure 5 are given in Tables S6 and S7 in the SI.

4.1.3. Binol. Binol (1,1′-bis-2-naphthol) is an axially chiral compound composed of two naphthol moieties connected by a single bond. The two atropoisomers are labeled either R_a/S_a or *P*/*M*. Here, we considered two structures: the ground-state optimized structure (S_0) of the S_a enantiomer taken from ref 43, where the dihedral angle between the two moieties is ∼90° ("orthogonal" conformation) and the S_0 of the R_a enantiomer taken from the recent computational study at the ADC level of theory,[45] which is a DFT/CAM-B3LYP/cc-pVTZ optimized structure. A symmetrized version of the latter was also employed for computational efficiency, after validating that the two structures yield equivalent results. The steady-state and time-resolved ECD spectra of binol have been measured by Hache and co-workers in different solvents.[39,43,84] Niezborala and Hache report the steady-state spectrum of *R*-binol in ethanol, whereas the one of *S*-binol in cyclohexane was reported by Schmid et al.[43]

Electronic transitions in binol are often labeled using the Platt nomenclature relative to the 2-naphthol precursor. The first two bright transitions are called L_a and L_b, where L_a is the more intense one (HOMO → LUMO character). The relative ordering of the L_a and L_b transitions is method dependent. At the EOM-CCSD/6-31G(d) level, the lowest excited state of isolated 2-naphthol is L_b at 4.45 eV (f^{lg} = 0.02), whereas the second, at 5.39 eV (f^{lg} = 0.06), is L_a. They are followed by a third state at 6.28 eV (f^{lg} = 0.04). An intense *B* state (according to Platt's notation) comes as fourth at 6.60 eV (f^{lg} = 1.29). With the cc-pVDZ basis, we obtain the excited states at 4.40 eV (f^{lg} = 0.02); 5.26 eV (f^{lg} = 0.047); 6.19 eV (f^{lg} = 0.033); 6.49 eV (f^{lg} = 1.21). At the TDDFT level, the ordering of the two states is reversed, with L_a dropping below L_b.

This different ordering carries over to binol. Exciton pairs are obtained from the combination of the L_a and L_b states of the two naphthol moieties. The lowest EOM-CCSD exciton pair comprises the two states, respectively at 4.42 eV (f^{lg} = 0.052) and 4.44 eV (f^{lg} = 0.012) in the 6-31G(d) basis, which are labeled L_b-1 (of B symmetry) and L_b-2 (of A symmetry). The states of the second exciton pair, of L_a character, are at 5.29 eV (f^{lg} = 0.20, L_a-1, B symmetry) and 5.33 eV (f^{lg} = 0.012, L_a-2, A symmetry). At the TDDFT/CAM-B3LYP level, the first exciton pair corresponds to L_a-1 (4.44 eV, f^{lg} = 0.14) and L_a-2 (4.48 eV, f^{lg} = 0.02); the second pair is L_b-1 (4.86 eV; f^{lg} = 0.10) and L_b-2 (4.86 eV; f^{lg} = 1.0×10^{-4}). We summarize in Table 1 our results for energies, oscillator strengths, and rotatory strengths of the L_a and L_b states of the R_a and S_a structures considered here, using EOM-CCSD and CAM-B3LYP and two different basis sets.

Table 1. First Four Excited States of Binol According to CCSD and CAM-B3LYP (Rotatory Strengths in 10^{-40} cgs)

	E (eV)	f	State/ Sym	Label	R^{lg}	R^{vg}
S_a-binol/6-31G(d)						
CCSD	4.42	0.05	1/B	L_b-1	20.44	7.26
	4.44	0.01	1/A	L_b-2	−37.52	−20.21
	5.29	0.20	2/B	L_a-1	−0.86	1.32
	5.33	0.01	2/A	L_a-2	−25.95	−17.39
CAM-B3LYP	4.44	0.14	1/B	L_a-1	33.91	31.46
	4.48	0.02	1/A	L_a-2	−80.89	−73.08
	4.86	0.10	2/B	L_b-1	4.11	2.83
	4.86	0.00	2/A	L_b-2	−0.835	−1.06
R_a-binol/cc-pVDZ						
CCSD	4.42	0.06	1/B	L_b-1	−16.93	−5.01
	4.44	0.01	1/A	L_b-2	37.49	21.55
	5.22	0.18	2/B	L_a-1	3.43	0.33
	5.26	0.01	2/A	L_a-2	18.69	12.63
CAM-B3LYP	4.42	0.15	1/B	L_a-1	−23.27	−25.03
	4.47	0.02	1/A	L_a-2	66.62	71.98
	4.85	0.09	2/B	L_b-1	−1.05	−2.05
	4.86	0.00	2/A	L_b-2	0.43	0.31

Thus, in comparing the ES-ECD of the excited states of binol for the two methods, one should keep in mind that the character of the first excited state is different at the EOM-CCSD and CAM-B3LYP levels.

Figure 6 shows the EOM-CCSD GS- and ES-ECD spectra of S_a-binol, together with the experimental data from ref 43 (measured in cyclohexane). The ES-ECD were computed for all four lowest excitations in Table 1, plus the 5A and 5B (B_b-1 and B_b-2) states. Raw data are given in Tables S9, S10, and S11. Table S12 contains natural transition orbitals (NTOs) and transition properties of the four lowest GS transitions. The corresponding data for the R_a conformation are given in SI, see Tables S14−S16.

The EOM-CCSD GS-ECD spectra of binol agree well with the experimental results of refs 84 (R_a) and 43 (S_a), despite the neglect of solvent effects. Curiously, the split band at 6 eV in the experimental spectrum of R_a (reproduced by the calculations) is absent in the experimental spectrum of S_a. Both CAM-B3LYP (this work, as well as ref 43) and ADC(2) (ref 45) also agree with the experimental data.

Turning our attention to the ES-ECD spectra, the first general observation is that we could not reproduce the CAM-B3LYP results for the ES-ECD of S_a-binol reported in the SI of ref 43. Our CAM-B3LYP results are shown in Figure S4. Since our results for methyloxirane and norcamphor are consistent with CAM-B3LYP data reported by other authors, we suspect there may be a problem in the results reported by Schmid et al.

According to our calculations, the A and B symmetry excitation pairs have ES-ECD that are almost mirror images of each other across the x-axis. In the lower-energy region, the agreement between the length (origin at center-of-charge) and velocity gauges becomes poorer, as it can be appreciated from the results in Tables S10−S11 and from Figure S4. Our TD-DFT results show the same trend, see Figure S5.

Given the differences between length and velocity ES rotatory strengths at lower energies, we examined the gauge-origin dependence of the ES-ECD of the L_b-1 and L_b-2 states of S_a-binol. The gauge origin was manually located at an arbitrary carbon atom. The data reported in Table S13 show that it is only the rotatory strengths for transitions between different symmetries that are affected by the change of gauge origin. Overall, the effect of this shift of origin is fairly small, and it did neither significantly improve nor worsen the agreement between the two gauges. It could be interesting to test the effect of locating the gauge origin at the center-of-mass (or -charge) of the two naphthol moieties, respectively, but we have not pursued it here.

4.2. X-ray Circular Dichroism. *4.2.1. Methyloxirane.* The experimental XCD spectrum at the carbon K-edge of methyloxirane, measured in vapor phase, has been reported by Turchini et al.[85] and by Alberti et al.[86] Computational results at different levels of theory have also been reported.[33,87,88] A later study by Piancastelli et al.[89] focused on the nonchiral core-level photoelectron spectroscopy, the XAS at both C and O K-shells, and on resonant and normal Auger spectroscopies.

As explained by Turchini et al., a complicating factor in XCD measurements is that, to the first approximation, the magnetic dipole transition element of K-edge excitations is zero, since magnetic dipole transitions arising from s orbitals are forbidden. Consequently, the only possible source of magnetic dipole intensity involves 1s−np (particularly, 1s−2p) mixing. Theoretical studies[87,90] had indicated that this mixing could be sufficient to produce observable CD for simple organic molecules.

In the experimental measurement of Turchini et al., a nonlinear sloping background was present in the XCD of the two isomers, as well as their racemate, indicated as $[S(-) + R(+)]$. To obtain a monosignate signal, the measured spectra of the two enantiomers were halved and algebraically subtracted. This yielded the *composite* spectrum, labeled as $S(-)_c$, of $S(-)$-methyloxirane without the baseline background, since $S(-)_c = S(-)_m - \frac{1}{2}[S(-) + R(+)]_m = \frac{1}{2}[S(-)_m - R(+)_m]$ (where the subscript m stands for *measured*). Turchini et al. assigned the CD spectrum to the methyne and methylene carbon atoms (i.e., the oxygen-bound ones) and suggested that the methyl carbon's CD signal would essentially cancel out to zero because of the small energy splitting and the resolution of the experiment. A photoemission experiment revealed three binding energies of 291.2, 292.2, and 292.6 eV. With the d-aug-cc-pVDZ basis set, the three lowest ionization energies are 293.5, 294.8, and 294.9 eV, whereas with the d-aug-cc-pVTZ basis set the IEs are 291.3, 292.6, and 292.7 eV.

The simulation of the XCD (and XAS) spectra of methyloxirane proved to be rather challenging. We explored

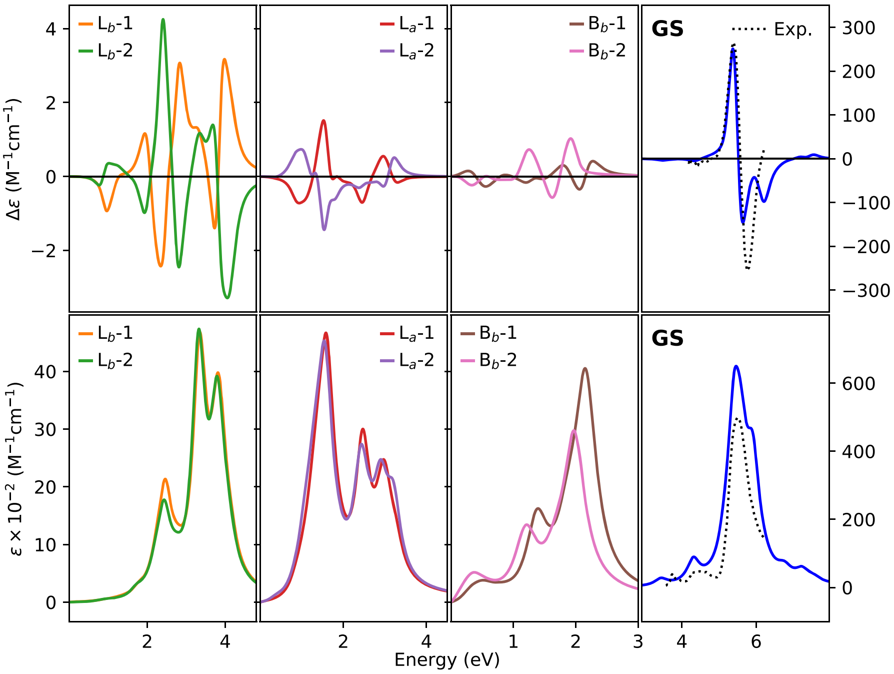

Figure 6. S_a-binol. Ground-state (GS) and excited-state (L_a, L_b, and B_b states) absorption (bottom panels) and ECD (upper panels) spectra in the length gauge computed at the EOM-CCSD/6-31G(d) level. Twenty excitations were considered in each irrep of the C_2 point group. Experimental values from ref 43. The CCSD energies have been shifted by −0.9 eV to align the main peaks in the experimental OPA spectrum. Lorentzian broadening with HWHM = 0.2 eV.

different basis sets, including d-aug-cc-pVDZ and d-aug-cc-pVTZ on all atoms, aug-cc-pVTZ on the C and O atoms and aug-cc-pVDZ on the H atoms, as well as Pople's 6-311++G** and 6-311(2+,+)G**, also uncontracting the inner functions. Two different optimized structures were considered. Comparisons between EOM-CCSD and CCSD-RSP results were carried out. Note that we report results for the *R* enantiomer, whereas the XCD spectra of ref 11 refer to the *S* enantiomer.

The simulated spectra for two different structures (yielded by EOM-CCSD and CC-RSP using the 6-311++G** basis set) are shown in Figure 7, along with experimental results. EOM-CCSD and CCSD-RSP results are consistent, though with a few noticeable differences in the XCD intensity in the length gauge. The moderate differences between velocity and length XCD results depend, to a certain extent, on the absolute size of the rotatory strength, as transitions with extremely small rotatory strengths sometimes have oppositely signed strengths.

The spectra stem from a number of closely lying excitations, whose rotatory strengths may significantly vary with the basis set. The spectra computed for the two optimized equilibrium geometries considered here show large differences. For the structure labeled "Geometry 2" in Figure 7, which is the one from ref 44 also used for ES-ECD, the excited states are less clustered, so the XAS spectral features are more smeared out. The most dramatic difference is, however, observed in the XCD spectra, where the first negative and weak broad band is replaced by a positive one, and the second negative one is far more pronounced. Changing the basis also affects the spectra, as illustrated in Figure 8 for "Geometry 1" (the MP2 optimized structure from ref 76).

The computed XAS spectra agree with the experiments, with overall energy shifts that vary between 0.06 and 2.3 eV, depending on the basis set. The shifts were computed with respect to the first peak of the spectrum of Piancastelli et al. Clearly identifiable XCD spectral patterns are reproduced by all basis sets and for both geometries, yet strikingly different from the measured ones. Given the results, we cannot conclude whether there is a problem with the measured XCD spectrum or whether the differences are due to deficiencies in our simulation. One possible reason for discrepancy is that our calculations do not include dynamical sampling of the structures. We note in passing, though, that the computed rotatory strengths Turchini et al.[85] report as taken from ref 88 do not appear to correspond to the values tabulated in ref 88. Also, to the best of our understanding, the calculation of ref 88 was carried out on the *R* isomer and not the *S* one.

It is important to identify the origin of the main peaks in our spectra. Inspection of the NTOs reveals that all three carbon atoms are optically active, in agreement with ref 87. In the 6-311++G** basis, the first XAS transition at Geometry 1 (287.5 eV) is due to the methyl C ("C3"), which is dark in XCD. The second and third electronic transitions combine to form the broad feature around 288.5 eV, which changes sign across the two geometries. The two transitions originate both from C3. Three excitations are responsible for the following (negative) band, the one with the largest (negative) rotatory strength coming from the nonchiral oxygen-bound C ("C2"). The next, positive, peak (at around 289.5 eV) stems from two transitions, both with positive rotatory strength, the first one from the chiral center C ("C1"), and the next one from C3. The following negative feature originates mainly from the net balance of two closely lying and oppositely signed sticks at Geometry 1, one positive from C2 and one negative from C1, whereas at Geometry 2 this feature comes from two negative sticks, the strongest due to C2. The positive band at around 290 eV is a convolution of several transitions, from all three carbon atoms.

The first broad band in the XCD spectra of both geometries is, as mentioned, due to two excitations from only the methyl carbon. This is also the band that changes sign between the

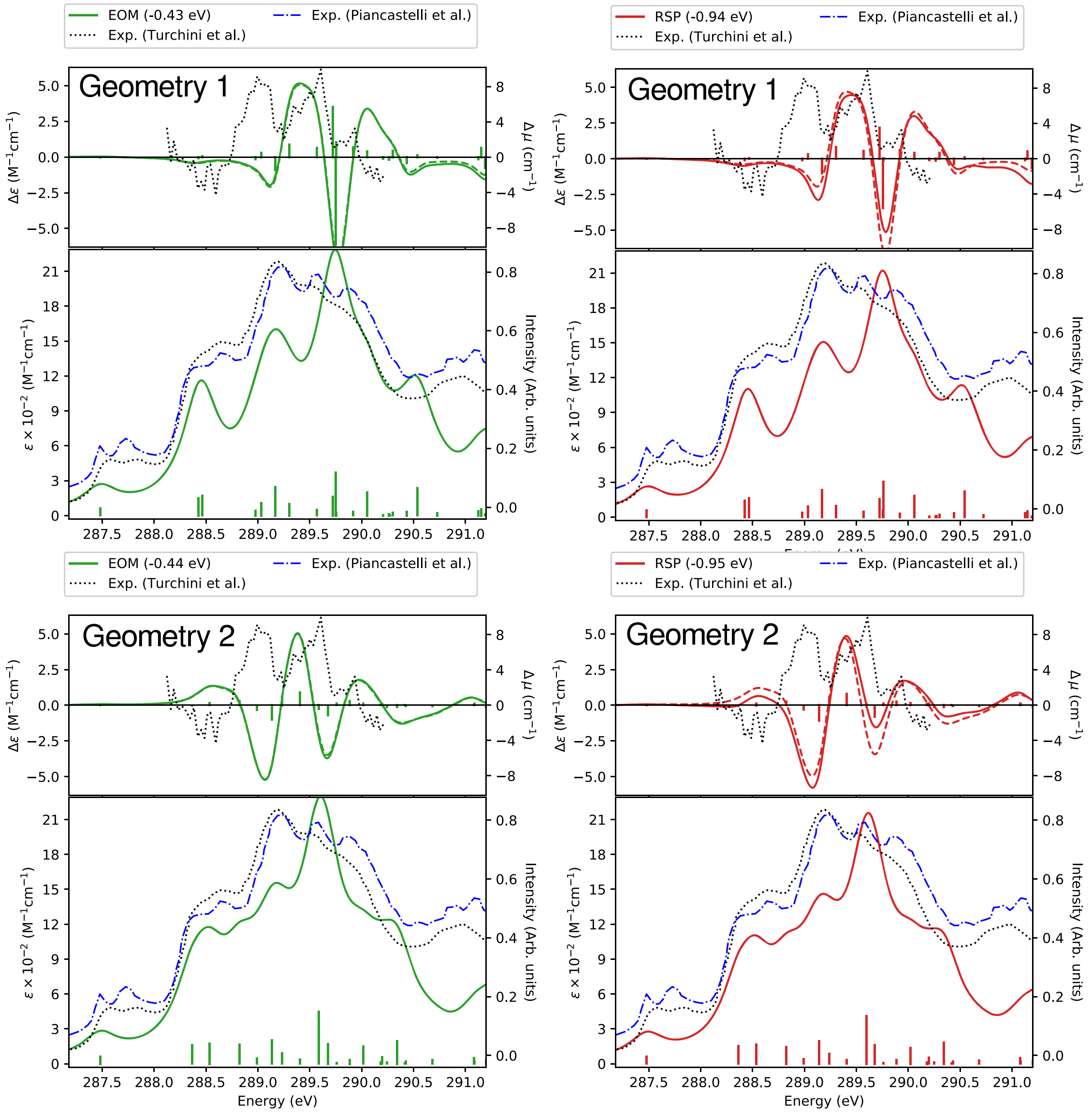

Figure 7. (*R*)-Methyloxirane. Carbon *K*-edge XCD (upper panels) and XAS (bottom panels) spectra at two different ground-state optimized geometries. Basis set 6-311++G**. Length gauge pictured in solid line, velocity in dashed. Experimental XAS[85,86,89] and XCD[85,86] are also shown. The experimental XCD of the *S* enantiomer is here reported as its mirror image. Lorentzian broadening with HWHM = 0.2 eV.

two geometries. It is therefore possible that a conformational average, which takes into account the group's free rotation, would result in a net zero contribution from these C3 excitations. However, at higher energies, excitations from C3 do not appear to cancel out.

4.2.2. L-Alanine. The XCD of alanine has previously been theoretically investigated using the STEX approach, the RPA method, as well at the complex polarization propagator (CPP) approach at the TDDFT/CAM-B3LYP level of theory.[91−93] A basis-set study[92] highlighted a strong basis-set dependence of the rotatory strengths, especially for the oxygen and nitrogen *K*-edges.

We calculated the XAS and XCD spectra at all three edges (carbon, oxygen, and nitrogen). The computed rotatory strengths are in general small and therefore sensitive to the convergence threshold adopted. Even with thresholds as tight as 10^{-7} (or even 10^{-8}), in particular, the oxygen-edge *R* values showed some variations. The results obtained with 10^{-7} are discussed below.

Our XAS and XCD spectra are illustrated in Figures 9 (C and O) and 10 (N). Raw spectral data for all figures can be found in Tables S27−S31 in the SI. NTOs of the main transitions are shown in Tables S32 and S33.

The computed carbon XAS of the neutral structure shows one dominating peak (third excited state) at 290.75 eV (f^{lg} = 0.076). This corresponds to a transition from the 1*s* orbital of C2 into the π^* of the carboxyl group (see Figure 1 for atom labeling). The majority of the computed states are transitions from the methyl carbon. It is the equivalent C 1*s* → π^* transition that dominates the carbon XAS spectrum of the zwitterion at 291.18 eV (f^{lg} = 0.066).

The oxygen XAS spectrum of the neutral structure has a simple profile with one major peak as the first transition at 536.45 eV (f^{lg} = 0.039) with the second transition at 3 eV higher in energy. The lowest transition occurs between the 1*s*

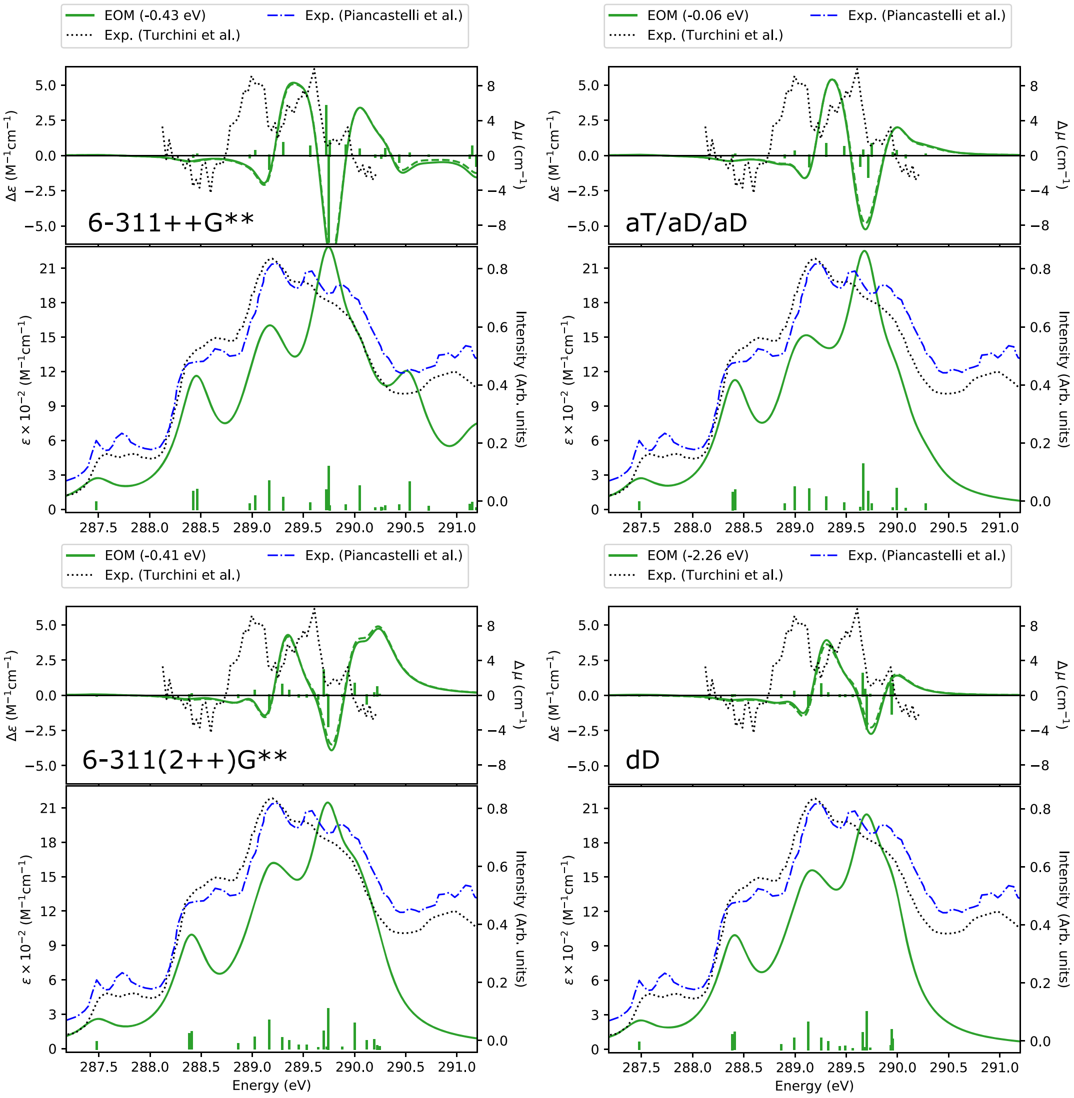

Figure 8. (R)-Methyloxirane. EOM-CCSD Carbon K-edge XCD (upper panels) and XAS (bottom panels) spectra with different basis sets (Geometry 1). The short notation dD stands for d-aug-cc-pVDZ; aT/aD/aD means aug-cc-pVTZ on the C atoms and aug-cc-pVDZ on the remaining atoms. Length gauge pictured in solid line, velocity in dashed. Experimental XAS[85,86,89] and XCD[85,86] are also shown. The experimental XCD of the S enantiomer is here reported as its mirror image. Lorentzian broadening with HWHM = 0.2 eV.

orbital of the doubly bonded oxygen (O2) into the π^*_{COOH} orbital. The corresponding transition from the protonated oxygen atom (O1) gives rise to the third peak observed in the spectrum. The second peak, i.e., the first in the split band, is due to a 1s transition from O2 into a p-type oxygen orbital. In the zwitterion, the carboxyl group is deprotonated, making the two oxygen atoms nearly equivalent. The oxygen K-edge XAS spectrum of the zwitterion shows two close-lying peaks of equal magnitude belonging to the O 1s → $\pi^*_{\mathrm{COO^-}}$ transitions. The first transition at 536.55 eV ($f^{\mathrm{lg}} = 0.029$) is from the O1 1s orbital, and the fourth transition (second peak) at 536.89 eV (f^{lg} = 0.029) originates from the O2 1s orbital. Two almost dark excitations lie between the O 1s → $\pi^*_{\mathrm{COO^-}}$ transitions. The first peak of the nitrogen XAS spectrum of both neutral and zwitterionic L-alanine arises from a transition from the N 1s into a diffuse orbital very localized around the N atom. For the second spectral peak for both forms, the particle orbital is of $\sigma^*_{\mathrm{N-H}}$ character. For the neutral form, the trailing transitions are weak and diffuse. The third peak in the zwitterion spectrum is due to a transition into an orbital localized around the N atom with slight $\sigma^*_{\mathrm{N-H}}$ character. The feature in the high-energy region arises from a transition into the $\sigma^*_{\mathrm{N-C}}$ orbital.

The XCD results indicate that all carbon atoms are optically active for both structures, where the majority of transitions are from the methyl carbon 1s orbital. At this K-edge, length and velocity gauge results are rather similar. At the nitrogen and oxygen K-edges, pronounced disagreement between the two gauges (length and velocity) is observed. In the nitrogen case, for instance, the velocity-gauge rotatory strengths are orders of magnitude smaller than the corresponding strengths in the length gauge. The large difference could be due to strong origin dependence of the rotatory strengths. To investigate this further, we tried moving the gauge origin to different locations. In the case of the N K-edge, we moved the origin on the nitrogen atom. The XCD spectra at the default and shifted origins are depicted in Figure 10. The effect of the origin shift from the center of charge to the N atom is striking, leading to almost complete overlap of the length and velocity gauge XCD

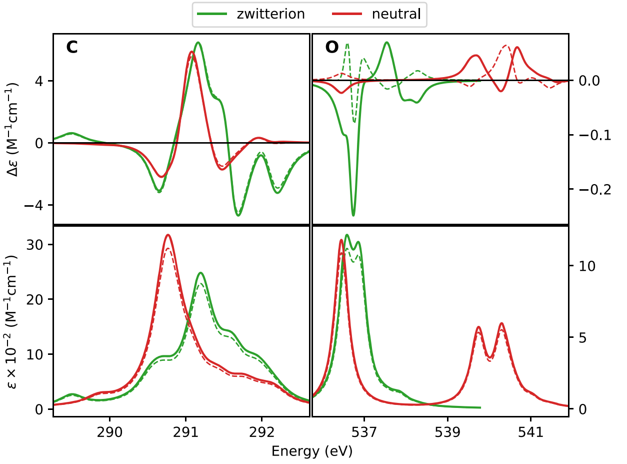

Figure 9. L-Alanine in its neutral and zwitter-ionic forms. Carbon (left, 12 states) and oxygen (right, 10 states) fc-CVS-EOM-CCSD/d-aug-cc-pVDZ *K*-edge XAS (bottom panels) and XCD (upper panels). Length gauge in solid lines; velocity in dashed. Lorentzian broadening with HWHM = 0.2 eV.

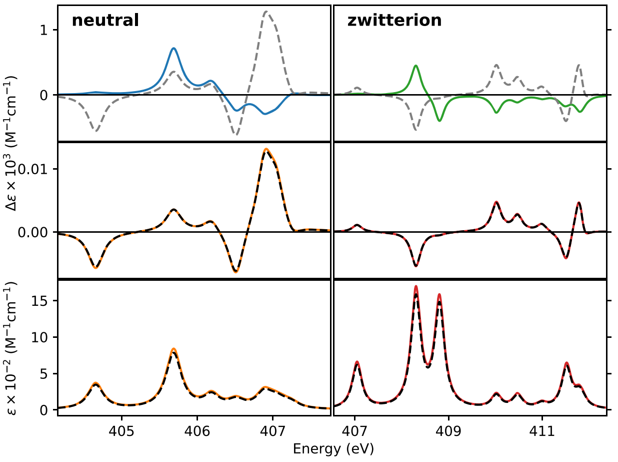

Figure 10. L-Alanine in its neutral and zwitter-ionic forms. Nitrogen *K*-edge fc-CVS-EOM-CCSD/d-aug-cc-pVDZ XAS (bottom panels) and XCD (upper and middle panels) spectra. Length gauge in solid lines; velocity in dashed. The top row shows the XCD with gauge origin in the center of charge; the middle row the ones with gauge origin at the position of the nitrogen atom. The spectra in gray (top panels) have been magnified by 10^2. Lorentzian broadening with HWHM = 0.125 eV.

spectra. A closer look at the NTOs of the N 1*s* transitions reveals that these transitions are highly localized on the N atom. We note, however, that the rotatory strength values are very small, so it remains a general concern whether the agreement after the gauge-origin shift of the length gauge is the mere consequence of having computed equally small residual errors in the two gauges. As an additional test, we carried out calculations on the neutral D-isomer (geometry produced by mirroring the L-structure in the *xy* plane). This produced the exact mirror image of the L-alanine N *K*-edge XCD spectra at both gauge origins.

Two shifted origins were tested for the O *K*-edge of neutral L-alanine: one at the doubly bonded oxygen atom and one at the center of mass of the carboxyl moiety. While applying these gauge shifts does have an impact on the oxygen *K*-edge XCD spectrum, it is not as clear-cut as for the nitrogen *K*-edge XCD. A nice overlap between the gauges was, however, obtained for some of the bands, e.g., the first peak in the XCD spectrum, when the origin is located at the doubly bonded oxygen atom. XCD spectra from the gauge-dependence study are shown in Figure S7.

Comparing the XCD spectra of this work with the ones simulated with the CPP/CAM-B3LYP/d-aug-cc-pVDZ method reported in ref 93, we observe that the N *K*-edge spectra of the neutral structures have similar features for the two methods, if one considers the gauge-shifted EOM-CCSD one. Meanwhile, the corresponding spectra of the zwitterion are quite different, although slight similarity can be found between the TD-DFT spectrum and the CCSD one with center-of-charge origin. The computed XAS spectra are similar. The oxygen XCD spectra of the zwitterionic structure are very different at any gauge origins. Note that we here used the structure of the Ala-I conformer fully optimized at the CCSD(T) level from ref 94, whereas a B3LYP optimized structure was used in ref 93.

4.2.3. Chloroethanol.

Inspired by ref 80, where chloroethanol was used as an illustrative case for XCD of larger chloro-compounds, we considered the chlorine $L_{2,3}$-edge XCD, focusing on the effect of spin−orbit coupling.

At the *L*-edge, the core transitions occur from the 2*p* orbitals of the targeted atom. The degeneracy of the three *p*-orbitals is split by the SOC, which is clearly seen in the X-ray absorption spectra. This splitting is expected to be observed in the XCD spectra as well.

Some of us recently reported an extension of EOM-CCSD for computation of *L*-edge XAS (and XPS) spectra,[69] employing a state-interaction two-step scheme. First, a set of nonrelativistic EOM-CC states is computed and used to evaluate SOCs using Breit−Pauli operator and mean-field approximation of the two-electron part, as described in refs 95 and 96. Then the resulting SOC-perturbed Hamiltonian matrix is diagonalized, giving rise to SOC-mixed states. Using the computed transformation between zero-order and SOC-perturbed states, the non-Hermitian electric dipole transition strengths are then transformed into a basis of SOC-split states, according to

$$\bar{S}_\alpha^{nf} = \mathbf{U}^\dagger \langle \hat{\mu}_\alpha^{nf} \rangle \langle \hat{\mu}_\alpha^{fn} \rangle \mathbf{U} \tag{46}$$

where the matrix **U** contains the eigenvectors of the spin−orbit mean-field Hamiltonian matrix. In the present work, the property of interest is the CD rotatory strength, so we considered the (anti)symmetrized product of the electric dipole and magnetic dipole transition moments (eq 18):

$$\bar{R}_\alpha^{nf} = \frac{1}{2}\mathbf{U}^\dagger \{\langle \hat{r}_\alpha^{nf} \rangle \langle \hat{L}_\alpha^{fn} \rangle - \langle \hat{L}_\alpha^{nf} \rangle \langle \hat{r}_\alpha^{fn} \rangle\} \mathbf{U} \tag{47}$$

and, likewise, for the velocity formulation (eq 19). Ten singlet excited states were computed for nonrelativistic transition properties, and equally many singlet and (spin-flip) triplet states were computed for the SOC calculations.

As for the nitrogen and oxygen *K*-edge XCD signals of alanine, we observe strong origin dependence of the *L*-edge XCD spectrum of chloroethanol. The simulated signals in the length gauge with gauge origin at the center of charge are an order of magnitude larger than the velocity-gauge equivalents. Shifting the origin from the center of charge to the chlorine atom improves the agreement between the two gauges significantly. The numerical values of the computed signals are very small, especially in the velocity gauge and in the length gauge with origin on Cl. Figure 11 shows the nonrelativistic and SOC spectra for gauge origin at the Cl atom. Figure S8 in the SI illustrates the gauge effect. Raw data are given in Table S31 in the SI.

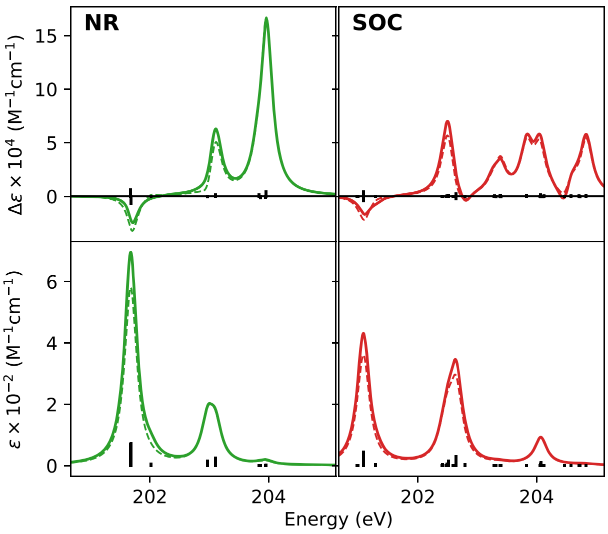

Figure 11. L-Chloroethanol. fc-CVS-EOM-CCSD/6-311(2+,+)G** nonrelativistic (NR, 10 states) and SOC Cl $L_{2,3}$-edge XAS (bottom panels) and XCD (upper panels). Gauge origin on the Cl atom, dashed lines are velocity gauge. Geometry from ref 80. Lorentzian broadening with HWHM = 0.124 eV.

The nonrelativistic XAS spectrum shows two peaks separated by 1.3 eV. The first peak is a convolution of two near-degenerate excited states at 201.68 eV of the same magnitude. The NTOs reveal that these transitions are of $2p \rightarrow \sigma^*_{\text{C-Cl}}$ type for the $2p$ orbitals perpendicular to the C−Cl bond (see Table S35). Their rotatory strengths have opposite signs and nearly the same magnitude. The second peak comprises three states: two near-degenerate at 202.97 eV, both with weak CD signals (note the sign disagreement between length and velocity gauge results for one of the transitions), and a single state at 203.11 eV with a positive CD signal. The near-degenerate states are transitions from the two perpendicular $2p$-orbitals into diffuse orbitals, and the single state is a transition between the $2p$ orbital lying along the C−Cl bond into diffuse orbitals.

The introduction of SOC splits the XAS spectrum into three peaks, where the middle one contains contributions from both the up-shifted splitting of the lowest NR peak and down-shifted splitting from the highest NR peak. Introducing SOC into XCD results in a richer (but slightly less intense) spectrum, with the intense band at 204 eV in the NR redistributing over several peaks. The individual transitions in this region have both positive and negative rotatory strengths, but the overall XCD cross section remains positive.

5. CONCLUSION

We implemented a computational scheme for simulating optical rotation and circular dichroism spectra based on the EOM-CCSD framework in the Q-Chem package. We applied these new tools to calculate ground-state and excited-state circular dichroism spectra of the selected compounds. The circular dichroism spectra were computed for both valence excitations and for core excitations at the *K*- and *L*-edges. In the calculations of *L*-edge X-ray circular dichroism, spin−orbit effects were included via the state-interaction procedure.

We observed generally good agreement between the simulated spectra obtained from EOM-CCSD with those from response theory at the CCSD level, and from TDDFT/CAM-B3LYP calculations. The assessment of the accuracy of the XCD results proved challenging. For methyloxirane, the computed spectra at the C *K*-edge do not bear clear resemblance with the experimental ones. A strong origin dependence of the XCD in the length gauge was observed at the oxygen and nitrogen *K*-edges of L-alanine, as well as the chlorine $L_{2,3}$-edge in chloroethanol. When the transition is highly localized, locating the gauge origin at the atom of excitation improves the agreement between the spectra from origin-dependent length gauge and those from the velocity gauge. In the X-ray regime, all computed signals, especially for the ones with strong gauge dependence, are extremely small and possibly at the limit of what the methodology can reliably reproduce. Also, without further studies, one cannot determine whether the sign of the experimental spectrum is dominated by vibronic effects, such as the Herzberg−Teller borrowing mechanisms—an aspect that goes beyond the present approach.

APPENDIX: EXPRESSIONS FOR TRANSITION 1PDMS

For brevity, in the following subsections, the left and right amplitudes of target EOM-EE-CCSD and fc-CVS-EOM-EE-CCSD states do not carry the state indices *n* and *f*. The CCSD Λ amplitudes do not carry the state index 0.

EOM-EE-CCSD State ← CCSD State Transition

$$\gamma_{ia}^{f\leftarrow 0} = \sum_{jb} (t_{ij}^{ab} - t_i^b t_j^a) l_j^b - \sum_j \tilde{l}_{ji} t_j^a - \sum_b \tilde{l}^{ba} t_i^b \tag{48}$$

$$\gamma_{ai}^{f\leftarrow 0} = l_i^a \tag{49}$$

$$\gamma_{ji}^{f\leftarrow 0} = -\tilde{l}_{ij} - \sum_a l_i^a t_j^a \tag{50}$$

$$\gamma_{ab}^{f\leftarrow 0} = \tilde{l}^{ab} + \sum_i l_i^a t_i^b \tag{51}$$

CCSD State ← EOM-EE-CCSD State Transition

Here, *l* represents the amplitudes of CCSD Λ.

$$\begin{aligned}\gamma_{ia}^{0\leftarrow f} = {} & r_i^a + \sum_{jb} (\tilde{\tilde{r}}_{ij}^{ab} - \tilde{r}_i^b t_j^a - \tilde{r}_j^a t_i^b) l_j^b + \sum_{jb} (t_{ij}^{ab} - t_j^a t_i^b) Y_{jb} \\ & - \sum_k \tilde{\tilde{l}}_{ki} r_k^a - \sum_c \tilde{\tilde{l}}^{ca} r_i^c - \sum_j \tilde{l}_{ji} t_j^a - \sum_b \tilde{l}^{ba} t_i^b\end{aligned} \tag{52}$$

$$\gamma_{ai}^{0\leftarrow f} = r_0 l_i^a + Y_{ia} \tag{53}$$

$$\gamma_{ji}^{0\leftarrow f} = -\tilde{l}_{ij} - \sum_a l_i^a \tilde{\tilde{r}}_j^a - \sum_a Y_{ia} t_j^a \tag{54}$$

$$\gamma_{ab}^{0\leftarrow f} = \tilde{l}^{ab} + \sum_i l_i^a \tilde{\tilde{r}}_i^b + \sum_i Y_{ia} t_i^b \tag{55}$$

https://doi.org/10.1021/acs.jctc.1c00937
J. Chem. Theory Comput. 2022, 18, 1748−1764

EOM-EE-CCSD State *f* ← EOM-EE-CCSD State *n* Transition

$$\gamma_{ia}^{f\leftarrow n} = \sum_{jb} (\tilde{\tilde{r}}_{ij}^{ab} - \tilde{r}_i^b t_j^a - \tilde{r}_j^a t_i^b) l_j^b + \sum_{jb} (t_{ij}^{ab} - t_j^a t_i^b) Y_{jb} - \sum_k \tilde{\tilde{l}}_{ki} r_k^a - \sum_c \tilde{\tilde{l}}^{ca} r_i^c - \sum_j \tilde{l}_{ji} t_j^a - \sum_b \tilde{l}^{ba} t_i^b \tag{56}$$

$$\gamma_{ai}^{f\leftarrow n} = r_0 l_i^a + Y_{ia} \tag{57}$$

$$\gamma_{ji}^{f\leftarrow n} = -\tilde{l}_{ij} - \sum_a l_i^a \tilde{\tilde{r}}_j^a - \sum_a Y_{ia} t_j^a \tag{58}$$

$$\gamma_{ab}^{f\leftarrow n} = \tilde{l}^{ab} + \sum_i l_i^a \tilde{\tilde{r}}_i^b + \sum_i Y_{ia} t_i^b \tag{59}$$

fc-CVS-EOM-EE-CCSD State ← CCSD State Transition

$$\gamma_{jI}^{f\leftarrow 0} = -\tilde{\tilde{l}}_{Ij} - \sum_a l_I^a t_j^a \tag{60}$$

$$\gamma_{aI}^{f\leftarrow 0} = l_I^a \tag{61}$$

CCSD State ← fc-CVS-EOM-EE-CCSD State Transition

Here, l represents the amplitudes of CCSD Λ.

$$\gamma_{Ji}^{0\leftarrow f} = -\tilde{l}_{iJ} - \sum_a l_i^a r_J^a \tag{62}$$

$$\gamma_{Ia}^{0\leftarrow f} = r_I^a + \sum_{jb} (r_{Ij}^{ab} - r_I^b t_j^a) l_j^b - \sum_c \tilde{\tilde{l}}^{ca} r_I^c - \sum_j \tilde{l}_{jI} t_j^a \tag{63}$$

Intermediates

$$Y_{ia} = \sum_{jb} l_{ij}^{ab} r_j^b \tag{64}$$

$$\tilde{\tilde{r}}_{ij}^{ab} = r_{ij}^{ab} + r_0 t_{ij}^{ab} \tag{65}$$

$$\tilde{r}_i^a = r_i^a + \frac{1}{2} r_0 t_i^a \tag{66}$$

$$\tilde{\tilde{r}}_i^a = r_i^a + r_0 t_i^a \tag{67}$$

$$\tilde{\tilde{l}}_{ij} = \frac{1}{2} \sum_{kab} l_{ik}^{ab} t_{jk}^{ab} \tag{68}$$

$$\tilde{\tilde{l}}^{ab} = \frac{1}{2} \sum_{ijc} l_{ij}^{ac} t_{ij}^{bc} \tag{69}$$

$$\tilde{l}_{ij} = \frac{1}{2} \sum_{kab} l_{ik}^{ab} \tilde{\tilde{r}}_{jk}^{ab} \tag{70}$$

$$\tilde{l}^{ab} = \frac{1}{2} \sum_{ijc} l_{ij}^{ac} \tilde{\tilde{r}}_{ij}^{bc} \tag{71}$$

$$\tilde{\tilde{l}}_{Ij} = \frac{1}{2} \sum_{kab} l_{Ik}^{ab} t_{jk}^{ab} \tag{72}$$

$$\tilde{l}_{iJ} = \frac{1}{2} l_{ik}^{ab} r_{Jk}^{ab} \tag{73}$$

■ ASSOCIATED CONTENT

Supporting Information

The Supporting Information is available free of charge at https://pubs.acs.org/doi/10.1021/acs.jctc.1c00937.

> Additional information: Tables of raw data, Additional spectra, CAM-B3LYP results for Binol, Geometrical parameters. (PDF)

■ AUTHOR INFORMATION

Corresponding Author

Sonia Coriani − *DTU Chemistry, Technical University of Denmark, DK-2800 Kongens Lyngby, Denmark;* orcid.org/0000-0002-4487-897X; Email: soco@kemi.dtu.dk

Authors

Josefine H. Andersen − *DTU Chemistry, Technical University of Denmark, DK-2800 Kongens Lyngby, Denmark;* orcid.org/0000-0002-0534-7463

Kaushik D. Nanda − *Department of Chemistry, University of Southern California, Los Angeles, California 90089, United States;* orcid.org/0000-0002-3447-6678

Anna I. Krylov − *Department of Chemistry, University of Southern California, Los Angeles, California 90089, United States;* orcid.org/0000-0001-6788-5016

Complete contact information is available at: https://pubs.acs.org/10.1021/acs.jctc.1c00937

Notes

The authors declare the following competing financial interest(s): A.I.K. is the president and a part-owner of Q-Chem, Inc.

■ ACKNOWLEDGMENTS

J.H.A and S.C. thank Dr. Dirk Rehn (UHEI), Dr. Mikael Scott (UHEI), Dr. Evgeny Epifanovsky (Q-Chem), Dr. Fabrizio Santoro (CNR) and Dr. Roberto Improta (CNR) for useful discussions. The authors also acknowledge Dr. Pavel Pokhilko, who implemented the angular momentum integrals in Q-Chem. J.H.A and S.C. acknowledge financial support from the Independent Research Fund Denmark—Natural Sciences, Research Project 2, grant no. 7014-00258B. The Marie Skłodowska-Curie European Training Network "COSINE-COmputational Spectroscopy In Natural sciences and Engineering", Grant Agreement No. 765739, is also acknowledged. A.I.K. acknowledges support by the U.S. National Science Foundation (No. CHE-1856342).

■ REFERENCES

(1) Barron, L. D. *Molecular light scattering and optical activity*, 2nd ed.; Cambridge University Press: 2004.

(2) Mellin, G. W.; Katzenstein, M. The Saga of Thalidomide. *N. Engl. J. Med.* **1962**, *267*, 1184−1193.

(3) Davankov, V. A. Biological Homochirality on the Earth, or in the Universe? A Selective Review. *Symmetry* **2018**, *10*, 749.

(4) Berova, N., Nakanishi, K., Woody, R. W., Eds. *Circular Dichroism. Principles and Applications*, 2nd ed.; Wiley: New York, 2000.

(5) Warnke, I.; Furche, F. Circular dichroism: electronic. *WIREs Comput. Mol. Sci.* **2012**, *2*, 150−166.

(6) Nafie, L. A. Infrared and Raman Vibrational Optical Activity: Theoretical and Experimental Aspects. *Annu. Rev. Phys. Chem.* **1997**, *48*, 357−386.

(7) Microwave circular dichroism seen feasible. *Chemical & Engineering News Archive* **1986**, *64*, 16−17.

(8) Salzman, W. Circular Dichroism at Microwave Frequencies: Calculated Rotational Strengths for Transitions Up to J = 10 for Some Oxirane Derivatives. *J. Mol. Spectrosc.* **1998**, *192*, 61−68.

(9) Cameron, R. P.; Götte, J. B.; Barnett, S. M. Chiral rotational spectroscopy. *Phys. Rev. A* **2016**, *94*, 032505.

(10) Janssen, M. H. M.; Powis, I. Detecting chirality in molecules by imaging photoelectron circular dichroism. *Phys. Chem. Chem. Phys.* **2014**, *16*, 856−871.

(11) Turchini, S.; Zema, N.; Contini, G.; Alberti, G.; Alagia, M.; Stranges, S.; Fronzoni, G.; Stener, M.; Decleva, P.; Prosperi, T. Circular dichroism in photoelectron spectroscopy of free chiral molecules: Experiment and theory on methyl-oxirane. *Phys. Rev. A - At. Mol. Opt. Phys.* **2004**, *70*, 1−4.

(12) Pescitelli, G.; Bruhn, T. Good Computational Practice in the Assignment of Absolute Configurations by TDDFT Calculations of ECD Spectra. *Chirality* **2016**, *28*, 466−474.

(13) Guo, Y.; Ding, L.; Ghidinelli, S.; Gotfredsen, C. H.; de la Cruz, M.; Mackenzie, T. A.; Ramos, M. C.; Sánchez, P.; Vicente, F.; Genilloud, O.; Coriani, S.; Larsen, R. W.; Frisvad, J. C.; Larsen, T. O. Taxonomy Driven Discovery of Polyketides from Aspergillus californicus. *J. Nat. Prod.* **2021**, *84*, 979−985.

(14) Lin, N.; Forzato, C.; Berti, F.; Felluga, F.; Nitti, P.; Pitacco, G.; Coriani, S. On the Absolute Configuration of Chiral 1,4-Dihydropyridazines Synthesized by Organocatalysed Reactions. *J. Org. Chem.* **2013**, *78*, 11670−11679.

(15) Pecul, M.; Ruud, K. The Ab Initio Calculation of Optical Rotation and Electronic Circular Dichroism. In *Advances in Quantum Chemistry*; 2005; Vol. *50*; pp 185−212.

(16) Crawford, T. D.; Tam, M. C.; Abrams, M. L. The current state of ab initio calculations of optical rotation and electronic circular dichroism spectra. *J. Phys. Chem. A* **2007**, *111*, 12057−12068.

(17) Crawford, T. D.; Tam, M. C.; Abrams, M. L. The problematic case of (*S*)-methylthiirane: electronic circular dichroism spectra and optical rotatory dispersion. *Mol. Phys.* **2007**, *105*, 2607−2617.

(18) Helgaker, T.; Coriani, S.; Jørgensen, P.; Kristensen, K.; Olsen, J.; Ruud, K. Recent Advances in Wave Function-Based Methods of Molecular Property Calculations. *Chem. Rev.* **2012**, *112*, 543−631.

(19) Scott, M.; Rehn, D. R.; Coriani, S.; Norman, P.; Dreuw, A. Electronic circular dichroism spectra using the algebraic diagrammatic construction schemes of the polarization propagator up to third order. *J. Chem. Phys.* **2021**, *154*, 064107.

(20) Stanton, J. F.; Bartlett, R. J. The equation of motion coupled-cluster method. A systematic biorthogonal approach to molecular excitation energies, transition probabilities, and excited state properties. *J. Chem. Phys.* **1993**, *98*, 7029−7039.

(21) Bartlett, R. J. Coupled-cluster theory and its equation-of-motion extensions. *WIREs Comput. Mol. Sci.* **2012**, *2*, 126−138.

(22) Krylov, A. I. Equation-of-motion coupled-cluster methods for open-shell and electronically excited species: The hitchhiker's guide to Fock space. *Annu. Rev. Phys. Chem.* **2008**, *59*, 433−462.

(23) Coriani, S.; Pawlowski, F.; Olsen, J.; Jørgensen, P. Molecular response properties in equation of motion coupled cluster theory: A time-dependent perspective. *J. Chem. Phys.* **2016**, *144*, 024102.

(24) Koch, H.; Jørgensen, P. Coupled Cluster Response Functions. *J. Chem. Phys.* **1990**, *93*, 3333−3344.

(25) Christiansen, O.; Jørgensen, P.; Hättig, C. Response functions from Fourier component variational perturbation theory applied to a time-averaged quasienergy. *Int. J. Quantum Chem.* **1998**, *68*, 1−52.

(26) Nanda, K. D.; Krylov, A. I. Two-photon absorption cross sections within equation-of-motion coupled-cluster formalism using resolution-of-the-identity and Cholesky decomposition representations: Theory, implementation, and benchmarks. *J. Chem. Phys.* **2015**, *142*, 064118.

(27) Nanda, K. D.; Krylov, A. I. Visualizing the contributions of virtual states to two-photon absorption cross-sections by natural transition orbitals of response transition density matrices. *J. Phys. Chem. Lett.* **2017**, *8*, 3256−3265.

(28) Nanda, K. D.; Krylov, A. I. The effect of polarizable environment on two-photon absorption cross sections characterized by the equation-of-motion coupled-cluster singles and doubles method combined with the effective fragment potential approach. *J. Chem. Phys.* **2018**, *149*, 164109.

(29) Friese, D. H.; Hättig, C.; Rizzo, A. Origin-independent two-photon circular dichroism calculations in coupled cluster theory. *Phys. Chem. Chem. Phys.* **2016**, *18*, 13683−13692.

(30) Coriani, S.; Hättig, C.; Jørgensen, P.; Helgaker, T. Gauge-origin independent magneto-optical activity within coupled cluster response theory. *J. Chem. Phys.* **2000**, *113*, 3561−3572.

(31) Faber, R.; Ghidinelli, S.; Hättig, C.; Coriani, S. Magnetic circular dichroism spectra from resonant and damped coupled cluster response theory. *J. Chem. Phys.* **2020**, *153*, 114105.

(32) Vidal, M. L.; Feng, X.; Epifanovsky, E.; Krylov, A. I.; Coriani, S. A new and efficient equation-of-motion coupled-cluster framework for core-excited and core-ionized states. *J. Chem. Theory Comput.* **2019**, *15*, 3117−3133.

(33) Faber, R.; Coriani, S. Core−valence-separated coupled-cluster-singles-and-doubles complex-polarization-propagator approach to X-ray spectroscopies. *Phys. Chem. Chem. Phys.* **2020**, *22*, 2642−2647.

(34) Vidal, M. L.; Krylov, A. I.; Coriani, S. Dyson orbitals within the fc-CVS-EOM-CCSD framework: theory and application to X-ray photoelectron spectroscopy of ground and excited states. *Phys. Chem. Chem. Phys.* **2020**, *22*, 2693−2703.

(35) Faber, R.; Coriani, S. Resonant Inelastic X-ray Scattering and Nonresonant X-ray Emission Spectra from Coupled-Cluster (Damped) Response Theory. *J. Chem. Theory Comput.* **2019**, *15*, 520−528.

(36) Nanda, K.; Vidal, M. L.; Faber, R.; Coriani, S.; Krylov, A. I. How to stay out of trouble in RIXS calculations within the equation-of-motion coupled-cluster damped response theory framework? Safe hitchhiking in the excitation manifold by means of core-valence separation. *Phys. Chem. Chem. Phys.* **2020**, *22*, 2629.

(37) Pedersen, T. B.; Koch, H.; Boman, L.; Sánchez de Merás, A. M. Origin invariant calculation of optical rotation without recourse to London orbitals. *Chem. Phys. Lett.* **2004**, *393*, 319−326.

(38) Caricato, M. Origin invariant optical rotation in the length dipole gauge without London atomic orbitals. *J. Chem. Phys.* **2020**, *153*, 151101.

(39) Hache, F. Application of time-resolved circular dichroism to the study of conformational changes in photochemical and photobiological processes. *J. Photochem. Photobiol., A* **2009**, *204*, 137−143.

(40) Mendonça, L.; Hache, F.; Changenet-Barret, P.; Plaza, P.; Chosrowjan, H.; Taniguchi, S.; Imamoto, Y. Ultrafast carbonyl motion of the photoactive yellow protein chromophore probed by femtosecond circular dichroism. *J. Am. Chem. Soc.* **2013**, *135*, 14637−14643.

(41) Cireasa, R.; Boguslavskiy, A. E.; Pons, B.; Wong, M. C. H.; Descamps, D.; Petit, S.; Ruf, H.; Thiré, N.; Ferré, A.; Suarez, J.; Higuet, J.; Schmidt, B. E.; Alharbi, A. F.; Légaré, F.; Blanchet, V.; Fabre, B.; Patchkovskii, S.; Smirnova, O.; Mairesse, Y.; Bhardwaj, V. R. Probing molecular chirality on a sub-femtosecond timescale. *Nat. Phys.* **2015**, *11*, 654−658.

(42) Baykusheva, D.; Zindel, D.; Svoboda, V.; Bommeli, E.; Ochsner, M.; Tehlar, A.; Wörner, H. J. Real-time probing of chirality during a chemical reaction. *Proc. Natl. Acad. Sci. U. S. A.* **2019**, *116*, 23923−23929.

(43) Schmid, M.; Martinez-Fernandez, L.; Markovitsi, D.; Santoro, F.; Hache, F.; Improta, R.; Changenet, P. Unveiling Excited-State Chirality of Binaphthols by Femtosecond Circular Dichroism and Quantum Chemical Calculations. *J. Phys. Chem. Lett.* **2019**, *10*, 4089−4094.

(44) Rizzo, A.; Vahtras, O. Ab initio study of excited state electronic circular dichroism. Two prototype cases: Methyl oxirane and R-(+)-1,1'-bi(2-naphthol). *J. Chem. Phys.* **2011**, *134*, 244109.

(45) Scott, M.; Rehn, D. R.; Norman, P.; Dreuw, A. Ab Initio Excited-State Electronic Circular Dichroism Spectra Exploiting the

Third-Order Algebraic-Diagrammatic Construction Scheme for the Polarization Propagator. *J. Phys. Chem. Lett.* **2021**, *12*, 5132−5137.

(46) Kowalczyk, T. D.; Abrams, M. L.; Crawford, T. D. Ab Initio Optical Rotatory Dispersion and Electronic Circular Dichroism Spectra of (S)-2-Chloropropionitrile. *J. Phys. Chem. A* **2006**, *110*, 7649−7654.

(47) Skomorowski, W.; Pecul, M.; Sałek, P.; Helgaker, T. Electronic circular dichroism of disulphide bridge: Ab initio quantum-chemical calculations. *J. Chem. Phys.* **2007**, *127*, 085102.

(48) Nakai, Y.; Mori, T.; Inoue, Y. Theoretical and Experimental Studies on Circular Dichroism of Carbo[n]helicenes. *J. Phys. Chem. A* **2012**, *116*, 7372−7385.

(49) Fedotov, D. A.; Coriani, S.; Hättig, C. Damped (linear) response theory within the resolution-of-identity coupled cluster singles and approximate doubles (RI-CC2) method. *J. Chem. Phys.* **2021**, *154*, 124110.

(50) Koch, H.; Kobayashi, R.; Sanchez de Merás, A.; Jørgensen, P. Calculation of size-intensive transition moments from the coupled cluster singles and doubles linear response function. *J. Chem. Phys.* **1994**, *100*, 4393−4400.

(51) Caricato, M.; Trucks, G. W.; Frisch, M. J. On the difference between the transition properties calculated with linear response- and equation of motion-CCSD approaches. *J. Chem. Phys.* **2009**, *131*, 174104.

(52) Nanda, K. D.; Krylov, A. I.; Gauss, J. Communication: The pole structure of the dynamical polarizability tensor in equation-of-motion coupled-cluster theory. *J. Chem. Phys.* **2018**, *149*, 141101.

(53) Epstein, S. T. *The Variation Method in Quantum Chemistry*; Academic Press: New York, US, 1974.

(54) Hansen, A. E.; Bouman, T. D. Hypervirial relations as constraints in calculations of electronic excitation properties: the random phase approximation in configuration interaction language. *Mol. Phys.* **1979**, *37*, 1713−1724.

(55) Pedersen, T. B.; Koch, H. Gauge invariance of the coupled cluster oscillator strength. *Chem. Phys. Lett.* **1998**, *293*, 251−260.

(56) Helgaker, T.; Wilson, P. J.; Amos, R. D.; Handy, N. C. Nuclear shielding constants by density functional theory with gauge including atomic orbitals. *J. Chem. Phys.* **2000**, *113*, 2983−2989.

(57) Coriani, S.; Koch, H. Communication: X-ray absorption spectra and core-ionization potentials within a core-valence separated coupled cluster framework. *J. Chem. Phys.* **2015**, *143*, 181103.

(58) Tenorio, B. N. C.; Nascimento, M. A. C.; Rocha, A. B.; Coriani, S. Lanczos-based equation-of-motion coupled-cluster singles-and-doubles approach to the total photoionization cross section of valence excited states. *J. Chem. Phys.* **2019**, *151*, 184106.

(59) Norman, P.; Bishop, D. M.; Jensen, H. J. A.; Oddershede, J. Near-resonant absorption in the time-dependent self-consistent field and multiconfigurational self-consistent field approximations. *J. Chem. Phys.* **2001**, *115*, 10323−10334.

(60) Norman, P.; Bishop, D. M.; Jensen, H. J. A.; Oddershede, J. Nonlinear response theory with relaxation: The first-order hyperpolarizability. *J. Chem. Phys.* **2005**, *123*, 194103.

(61) Norman, P. A perspective on nonresonant and resonant electronic response theory for time-dependent molecular properties. *Phys. Chem. Chem. Phys.* **2011**, *13*, 20519−20535.

(62) Kristensen, K.; Kauczor, J.; Kjærgaard, T.; Jørgensen, P. Quasienergy formulation of damped response theory. *J. Chem. Phys.* **2009**, *131*, 044112.

(63) Kauczor, J.; Norman, P.; Christiansen, O.; Coriani, S. Communication: A reduced-space algorithm for the solution of the complex linear response equations used in coupled cluster damped response theory. *J. Chem. Phys.* **2013**, *139*, 211102.

(64) Stanton, J. F.; Gauss, J. Many-body methods for excited state potential energy surfaces. II. Analytic second derivatives for excited state energies in the equation-of-motion coupled cluster method. *J. Chem. Phys.* **1995**, *103*, 8931−8943.

(65) Nanda, K. D.; Krylov, A. I. Static polarizabilities for excited states within the spin-conserving and spin-flipping equation-of-motion coupled-cluster singles and doubles formalism: Theory, implementation, and benchmarks. *J. Chem. Phys.* **2016**, *145*, 204116.

(66) Nanda, K. D.; Krylov, A. I. The orbital picture of the first dipole hyperpolarizability from many-body response theory. *J. Chem. Phys.* **2021**, *154*, 184109.

(67) Shao, Y.; Gan, Z.; Epifanovsky, E.; Gilbert, A. T.; Wormit, M.; Kussmann, J.; Lange, A. W.; Behn, A.; Deng, J.; Feng, X.; Ghosh, D.; Goldey, M.; Horn, P. R.; Jacobson, L. D.; Kaliman, I.; Khaliullin, R. Z.; Kuś, T.; Landau, A.; Liu, J.; Proynov, E. I.; Rhee, Y. M.; Richard, R. M.; Rohrdanz, M. A.; Steele, R. P.; Sundstrom, E. J.; Woodcock, H. L.; Zimmerman, P. M.; Zuev, D.; Albrecht, B.; Alguire, E.; Austin, B.; Beran, G. J. O.; Bernard, Y. A.; Berquist, E.; Brandhorst, K.; Bravaya, K. B.; Brown, S. T.; Casanova, D.; Chang, C.-M.; Chen, Y.; Chien, S. H.; Closser, K. D.; Crittenden, D. L.; Diedenhofen, M.; DiStasio, R. A.; Do, H.; Dutoi, A. D.; Edgar, R. G.; Fatehi, S.; Fusti-Molnar, L.; Ghysels, A.; Golubeva-Zadorozhnaya, A.; Gomes, J.; Hanson-Heine, M. W.; Harbach, P. H.; Hauser, A. W.; Hohenstein, E. G.; Holden, Z. C.; Jagau, T.-C.; Ji, H.; Kaduk, B.; Khistyaev, K.; Kim, J.; Kim, J.; King, R. A.; Klunzinger, P.; Kosenkov, D.; Kowalczyk, T.; Krauter, C. M.; Lao, K. U.; Laurent, A. D.; Lawler, K. V.; Levchenko, S. V.; Lin, C. Y.; Liu, F.; Livshits, E.; Lochan, R. C.; Luenser, A.; Manohar, P.; Manzer, S. F.; Mao, S.-P.; Mardirossian, N.; Marenich, A. V.; Maurer, S. A.; Mayhall, N. J.; Neuscamman, E.; Oana, C. M.; Olivares-Amaya, R.; O'Neill, D. P.; Parkhill, J. A.; et al. Advances in molecular quantum chemistry contained in the Q-Chem 4 program package. *Mol. Phys.* **2015**, *113*, 184−215.

(68) Epifanovsky, E.; Gilbert, A. T. B.; Feng, X.; Lee, J.; Mao, Y.; Mardirossian, N.; Pokhilko, P.; White, A. F.; Coons, M. P.; Dempwolff, A. L.; Gan, Z.; Hait, D.; Horn, P. R.; Jacobson, L. D.; Kaliman, I.; Kussmann, J.; Lange, A. W.; Lao, K. U.; Levine, D. S.; Liu, J.; McKenzie, S. C.; Morrison, A. F.; Nanda, K. D.; Plasser, F.; Rehn, D. R.; Vidal, M. L.; You, Z.-Q.; Zhu, Y.; Alam, B.; Albrecht, B. J.; Aldossary, A.; Alguire, E.; Andersen, J. H.; Athavale, V.; Barton, D.; Begam, K.; Behn, A.; Bellonzi, N.; Bernard, Y. A.; Berquist, E. J.; Burton, H. G. A.; Carreras, A.; Carter-Fenk, K.; Chakraborty, R.; Chien, A. D.; Closser, K. D.; Cofer-Shabica, V.; Dasgupta, S.; de Wergifosse, M.; Deng, J.; Diedenhofen, M.; Do, H.; Ehlert, S.; Fang, P.-T.; Fatehi, S.; Feng, Q.; Friedhoff, T.; Gayvert, J.; Ge, Q.; Gidofalvi, G.; Goldey, M.; Gomes, J.; González-Espinoza, C. E.; Gulania, S.; Gunina, A. O.; Hanson-Heine, M. W. D.; Harbach, P. H. P.; Hauser, A.; Herbst, M. F.; Hernández Vera, M.; Hodecker, M.; Holden, Z. C.; Houck, S.; Huang, X.; Hui, K.; Huynh, B. C.; Ivanov, M.; Jász, A.; Ji, H.; Jiang, H.; Kaduk, B.; Kähler, S.; Khistyaev, K.; Kim, J.; Kis, G.; Klunzinger, P.; Koczor-Benda, Z.; Koh, J. H.; Kosenkov, D.; Koulias, L.; et al. Software for the frontiers of quantum chemistry: An overview of developments in the Q-Chem 5 package. *J. Chem. Phys.* **2021**, *155*, 084801.

(69) Vidal, M. L.; Pokhilko, P.; Krylov, A. I.; Coriani, S. Equation-of-Motion Coupled-Cluster Theory to Model *L*-Edge X-ray Absorption and Photoelectron Spectra. *J. Phys. Chem. Lett.* **2020**, *11*, 8314−8321.

(70) Faber, R.; Andersen, J. H.; Coriani, S. *py-ccrsp, Python module for CC and EOM-CC response experiments*. 2020−2021.

(71) Woon, D. E.; Dunning, T. H. Gaussian basis sets for use in correlated molecular calculations. III. The atoms aluminum through argon. *J. Chem. Phys.* **1993**, *98*, 1358−1371.

(72) Woon, D. E.; Dunning, T. H. Gaussian basis sets for use in correlated molecular calculations. V. Core-valence basis sets for boron through neon. *J. Chem. Phys.* **1995**, *103*, 4572−4585.

(73) Kendall, R. A.; Dunning, T. H.; Harrison, R. J. Electron affinities of the first-row atoms revisited. Systematic basis sets and wave functions. *J. Chem. Phys.* **1992**, *96*, 6796−6806.

(74) Aidas, K.; Angeli, C.; Bak, K. L.; Bakken, V.; Bast, R.; Boman, L.; Christiansen, O.; Cimiraglia, R.; Coriani, S.; Dahle, P.; Dalskov, E. K.; Ekström, U.; Enevoldsen, T.; Eriksen, J. J.; Ettenhuber, P.; Fernández, B.; Ferrighi, L.; Fliegl, H.; Frediani, L.; Hald, K.; Halkier, A.; Hättig, C.; Heiberg, H.; Helgaker, T.; Hennum, A. C.; Hettema, H.; Hjertenæs, E.; Høst, S.; Høyvik, I.-M.; Iozzi, M. F.; Jansík, B.; Jensen, H. J. Aa.; Jonsson, D.; Jørgensen, P.; Kauczor, J.; Kirpekar, S.; Kjærgaard, T.; Klopper, W.; Knecht, S.; Kobayashi, R.; Koch, H.;

Kongsted, J.; Krapp, A.; Kristensen, K.; Ligabue, A.; Lutnæs, O. B.; Melo, J. I.; Mikkelsen, K. V.; Myhre, R. H.; Neiss, C.; Nielsen, C. B.; Norman, P.; Olsen, J.; Olsen, J. M. H.; Osted, A.; Packer, M. J.; Pawlowski, F.; Pedersen, T. B.; Provasi, P. F.; Reine, S.; Rinkevicius, Z.; Ruden, T. A.; Ruud, K.; Rybkin, V. V.; Sałek, P.; Samson, C. C. M.; de Merás, A. S.; Saue, T.; Sauer, S. P. A.; Schimmelpfennig, B.; Sneskov, K.; Steindal, A. H.; Sylvester-Hvid, K. O.; Taylor, P. R.; Teale, A. M.; Tellgren, E. I.; Tew, D. P.; Thorvaldsen, A. J.; Thøgersen, L.; Vahtras, O.; Watson, M. A.; Wilson, D. J. D.; Ziolkowski, M.; Ågren, H. The Dalton quantum chemistry program system. *WIREs Comput. Mol. Sci.* **2014**, *4*, 269−284.

(75) Pokhilko, P.; Epifanovsky, E.; Krylov, A. I. Double Precision is Not Needed for Many-Body Calculations: Emergent Conventional Wisdom. *J. Chem. Theory Comput.* **2018**, *14*, 4088−4096.

(76) Cukras, J.; Kauczor, J.; Norman, P.; Rizzo, A.; Rikken, G. L. J. A.; Coriani, S. A complex-polarization-propagator protocol for magneto-chiral axial dichroism and birefringence dispersion. *Phys. Chem. Chem. Phys.* **2016**, *18*, 13267−13279.

(77) Sarangi, R.; Vidal, M. L.; Coriani, S.; Krylov, A. I. On the basis set selection for calculations of core-level states: different strategies to balance cost and accuracy. *Mol. Phys.* **2020**, *118*, No. e1769872.

(78) Olsen, J. M. H.; Reine, S.; Vahtras, O.; Kjellgren, E.; Reinholdt, P.; Hjorth Dundas, K. O.; Li, X.; Cukras, J.; Ringholm, M.; Hedegård, E. D.; Di Remigio, R.; List, N. H.; Faber, R.; Cabral Tenorio, B. N.; Bast, R.; Pedersen, T. B.; Rinkevicius, Z.; Sauer, S. P. A.; Mikkelsen, K. V.; Kongsted, J.; Coriani, S.; Ruud, K.; Helgaker, T.; Jensen, H. J. A.; Norman, P. Dalton Project: A Python platform for molecular- and electronic-structure simulations of complex systems. *J. Chem. Phys.* **2020**, *152*, 214115.

(79) Lehmann, M. S.; Koetzle, T. F.; Hamilton, W. C. Precision neutron diffraction structure determination of protein and nucleic acid components. I. Crystal and molecular structure of the amino acid L-alanine. *J. Am. Chem. Soc.* **1972**, *94*, 2657−2660.

(80) Zhang, Y.; Rouxel, J. R.; Autschbach, J.; Govind, N.; Mukamel, S. X-ray circular dichroism signals: a unique probe of local molecular chirality. *Chemical Science* **2017**, *8*, 5969−5978.

(81) Carnell, M.; Peyerimhoff, S.; Breest, A.; Gödderz, K.; Ochmann, P.; Hormes, J. Experimental and quantum-theoretical investigation of the circular dichroism spectrum of R-methyloxirane. *Chem. Phys. Lett.* **1991**, *180*, 477−481.

(82) Breest, A.; Ochmann, P.; Pulm, F.; Gödderz, K.; Carnell, M.; Hormes, J. Experimental circular dichroism and VUV spectra of substituted oxiranes and thiiranes. *Mol. Phys.* **1994**, *82*, 539−551.

(83) Pulm, F.; Schramm, J.; Hormes, J.; Grimme, S.; Peyerimhoff, S. D. Theoretical and experimental investigations of the electronic circular dichroism and absorption spectra of bicyclic ketones. *Chem. Phys.* **1997**, *224*, 143−155.

(84) Niezborala, C.; Hache, F. Conformational Changes in Photoexcited (*R*)-(+)-1,1'-Bi-2-naphthol Studied by Time-Resolved Circular Dichroism. *J. Am. Chem. Soc.* **2008**, *130*, 12783−12786.

(85) Turchini, S.; Zema, N.; Zennaro, S.; Alagna, L.; Stewart, B.; Peacock, R. D.; Prosperi, T. Core Electron Transitions as a Probe for Molecular Chirality: Natural Circular Dichroism at the Carbon *K*-edge of Methyloxirane. *J. Am. Chem. Soc.* **2004**, *126*, 4532−4533.

(86) Alberti, G.; Turchini, S.; Contini, G.; Zema, N.; Prosperi, T.; Stranges, S.; Feyer, V.; Bolognesi, P.; Avaldi, L. Dichroism in core-excited and core-ionized methyloxirane. *Phys. Scr.* **2008**, *78*, 058120.

(87) Alagna, L.; Di Fonzo, S.; Prosperi, T.; Turchini, S.; Lazzeretti, P.; Malagoli, M.; Zanasi, R.; Natoli, C. R.; Stephens, P. J. Random phase approximation calculations of *K*-edge rotational strengths of chiral molecules: propylene oxide. *Chem. Phys. Lett.* **1994**, *223*, 402−410.

(88) Carravetta, V.; Plachkevytch, O.; Vahtras, O.; Agren, H. Ordinary and rotatory intensities for X-ray absorption at the C 1*s* edge of organic chiral molecules: propylene oxide and trans-1,2-dimethylcyclopropane. *Chem. Phys. Lett.* **1997**, *275*, 70.

(89) Piancastelli, M. N.; Lischke, T.; Prümper, G.; Liu, X. J.; Fukuzawa, H.; Hoshino, M.; Tanaka, T.; Tanaka, H.; Harries, J.; Tamenori, Y.; Bao, Z.; Travnikova, O.; Céolin, D.; Ueda, K. Electronic structure of core-excited and core-ionized methyl oxirane. *J. Electron Spectrosc. Relat. Phenom.* **2007**, *156−158*, 259−264.

(90) Goulon, J.; Goulon-Ginet, C.; Rogalev, A.; Gotte, V.; Malgrange, C.; Brouder, C.; Natoli, C. R. X-ray natural circular dichroism in a uniaxial gyrotropic single crystal of $LiIO_3$. *J. Chem. Phys.* **1998**, *108*, 6394−6403.

(91) Plashkevych, O.; Carravetta, V.; Vahtras, O.; Ågren, H. Theoretical study of X-ray circular dichroism of amino acids. *Chem. Phys.* **1998**, *232*, 49−62.

(92) Kimberg, V.; Kosugi, N. Calculation of K-edge circular dichroism of amino acids: Comparison of random phase approximation with other methods. *J. Chem. Phys.* **2007**, *126*, 245101.

(93) Jiemchooroj, A.; Ekström, U.; Norman, P. Near-edge x-ray absorption and natural circular dichroism spectra of L-alanine: A theoretical study based on the complex polarization propagator approach. *J. Chem. Phys.* **2007**, *127*, 165104.

(94) Jaeger, H. M.; Schaefer, H. F.; Demaison, J.; Császár, A. G.; Allen, W. D. Lowest-Lying Conformers of Alanine: Pushing Theory to Ascertain Precise Energetics and Semiexperimental Re Structures. *J. Chem. Theory Comput.* **2010**, *6*, 3066−3078.

(95) Pokhilko, P.; Epifanovsky, E.; Krylov, A. I. General framework for calculating spin−orbit couplings using spinless one-particle density matrices: theory and application to the equation-of-motion coupled-cluster wave functions. *J. Chem. Phys.* **2019**, *151*, 034106.

(96) Epifanovsky, E.; Klein, K.; Stopkowicz, S.; Gauss, J.; Krylov, A. I. Spin-orbit couplings within the equation-of-motion coupled-cluster framework: Theory, implementation, and benchmark calculations. *J. Chem. Phys.* **2015**, *143*, 064102.